nature communications

Article

https://doi.org/10.1038/s41467-025-60853-8

# Injectable magnesium-bisphosphonate MOF-based bone adhesive prevents excessive fibrosis for osteoporotic fracture repair

Received: 20 November 2024

Accepted: 5 June 2025

Published online: 01 July 2025

Check for updates

Tianhua Xiao[1,2,3,7], Zunlei Gong[2,3,7], Dongming Duan[2,3], Hui Yu[2,3], Song Liu[2,3], Yuhe Jiang[4], Xudan Xing[2,3], Zenghui Wu[2,3], Le Wang[2,3], Xuebin B. Yang[5], Giuseppe Tronci[5], Chengyun Ning[6], Guoxin Tan[1] ✉ & Lei Zhou[2,3] ✉

Current treatments for osteoporotic fractures primarily target bone-resorbing osteoclasts, but they often fail to address fibrosis—a buildup of fibrous tissue that disrupts bone healing. This fibrosis is frequently triggered by bisphosphonates, which, while effective in reducing bone loss, also activate fibroblasts and impair callus formation. Here we show that an injectable hydrogel bone adhesive composed of magnesium-alendronate metal-organic frameworks (Mg-ALN MOF) embedded in a gelatin/dialdehyde starch network can simultaneously suppress bone resorption and reduce fibrosis. The Mg-ALN MOF adhesive binds firmly to irregular bone surfaces and degrades under acidic osteoporotic conditions, gradually releasing $Mg^{2+}$ ions. These ions competitively bind to sclerostin (SOST), thereby interrupting the SOST/TGF-β signaling pathway that promotes fibroblast activation and abnormal collagen deposition. This dual-action mechanism significantly enhances fracture healing, resulting in a 27.8% improvement in flexural strength. Our findings suggest a promising therapeutic strategy that combines mechanical support with targeted regulation of both bone resorption and pathological fibrosis.

With the aging population worldwide, osteoporosis (OP) has emerged as a major orthopedic degenerative disease characterized by excessive bone resorption[1]. This leads to decreased bone mass, impaired tissue microarchitecture, and reduced mechanical strength, making bones highly susceptible to fractures[2–4]. For instance, a hip fracture occurs every 3 s worldwide in patients showing signs of osteoporosis, which is approximately 9 million every year[5]. Bisphosphonates (BPs) are first-line anti-bone resorption medications that are most commonly used to prevent fracture and promote effective fracture healing[6]. However, BPs are characterized by high solubility and low permeability. This results in fairly low oral bioavailability (<1%), low gastrointestinal permeability, and severe side effects[7–9]. To overcome this limitation, biomaterials-based controlled delivery systems have acted as depots for the local delivery of active BPs medications to conform to the patient's needs and peculiarities[10]. Although these kinds of therapeutic platforms provide persistent biological restoration by locally inhibiting osteoclast activation, the side effects of being prone to the recurrence of fractures are still unavoidable. Long-term administration of BPs has been found to cause a new type of fracture known as atypical femur fractures (AFFs)[11]. Mortality rates following AFFs are 14% at 12

[1]School of Chemical Engineering and Light Industry, Guangdong University of Technology, Guangzhou, China. [2]Department of Orthopaedic Surgery, Guangzhou Key Laboratory of Spine Disease Prevention and Treatment, The Third Affiliated Hospital, Guangzhou Medical University, Guangzhou, China. [3]Guangdong Provincial Key Laboratory of Major Obstetric Diseases, Guangdong Provincial Clinical Research Center for Obstetrics and Gynecology, The Third Affiliated Hospital, Guangzhou Medical University, Guangzhou, China. [4]College of Osteopathic Medicine, New York Institute of Technology, New York, NY, USA. [5]School of Dentistry, St. James's University Hospital, University of Leeds, Leeds, UK. [6]School of Materials Science and Engineering, National Engineering Research Center for Tissue Restoration and Reconstruction, South China University of Technology, Guangzhou, China. [7]These authors contributed equally: Tianhua Xiao, Zunlei Gong. ✉e-mail: tanguoxin@126.com; zhoul@gzhmu.edu.cn

months and 25% at 24 months post-fracture[12]. The fundamental crux lies in the fact that not only the formation of osteoclasts is inhibited but also the differentiation of myeloid progenitor cells into fibroblasts is promoted, which results in excess fibrosis and impairs effective callus bridging.

Fibroblasts play a critical role in the early stages of bone healing by synthesizing extracellular matrix (ECM) components, including collagen, which contributes to the formation of granulation tissue and the soft callus that bridges the fracture site, facilitating cellular migration and vascularization[13,14]. However, excessive fibrosis, characterized by an overabundance of ECM and scar tissue, can impede fracture healing by restricting osteoblast differentiation and preventing proper mineralization and maturation of the callus. This pathological fibrosis can lead to delayed union or non-union of the fracture, impairing functional recovery[15,16]. Long-term BPs treatment has been demonstrated to promote the transition of progenitor cells into fibroblasts that actively deposit dense ECM, preventing fracture callus bridging[17]. Nevertheless, to the best of our knowledge, very few works have studied nonosteocytes such as fibroblasts on the effects of abnormal AFFs. Furthermore, there is a paucity of studies investigating how BPs and BPs-based biomaterials influence excessive fibrosis during fracture healing. Therefore, addressing the adverse effects of increased fibroblast activation and excessive fibrosis induced by BPs and revealing their therapeutic mechanisms are vitally important for further improvement of osteoporotic fractures repair.

Metal–organic frameworks (MOF) offer possibilities for the efficient delivery of multiple therapeutic agents to bone tissue and sustained release[18,19]. They can be prepared with organic linkers and metal centers with intrinsic bioactive and therapeutic properties, and they are expected to accomplish a better therapeutic outcome because of the combined and synergistic action between all elements[20]. Due to the pair of phosphate groups, BPs possess the capacity to bind metal ions via coordination bonds, thereby we took advantage of this feature to chelate it with metal ions and form multifunctional metal-BPs MOF. Transforming growth factor β (TGF-β) is a multifunctional cytokine that plays an important role in enhancing fibroblast migration and proliferation in different contexts acquiring an activated phenotype[21–24]. Previous studies have shown that BPs significantly upregulate TGF-β expression in mesenchymal stem cells (MSCs) or osteoblasts[25–27]. Mg has been reported to mitigate fibrosis and effectively reduce the transcriptional activation and expression of TGF-β[28–31]. With these findings in mind, we hypothesized that the Mg-BPs MOF would benefit the treatment of osteoporotic fractures by a combined strategy of simultaneously inhibiting osteoclast activation and reversing the adverse effects by attenuating fibrotic fibroblast activation.

Bone adhesives that form on injection into the injured bone tissue have recently been developed to treat bone fractures and make the treatment more convenient, faster, and safer than traditional internal fixation devices[32–37]. Here we show a multifunctional bioactive Mg-ALN MOF-based injectable hydrogel bone adhesive capable of locally inhibiting bone resorption and regulating fibrosis for initial fixation and later healing of fracture under osteoporotic conditions (Fig. 1a). The hydrogel forms through dynamic covalent bonding between catechol- and amine-rich highly branched gelatin (GND)/dialdehyde starch (DAS) network and Mg-ALN MOF, resulting in firm adhesion of the hydrogel to bone tissues. In this system, the ALN ligands can facilitate the accumulation of the MOF on the bone matrix due to the high binding affinity to hydroxyapatite mineral. In addition, Mg-ALN MOF acidity-responsively and sustainably release $Mg^{2+}$ and BPs over one month under osteoporotic acidic microenvironment. The osteoporotic fractures treated with these hydrogel bone adhesives exhibit rapid and fibrosis-preventing fractures healing by inhibiting osteoclast activation and the harmful effects of BPs-induced fibrosis. Mechanism studies reveal that the self-sacrificial release of $Mg^{2+}$ competitively binds to the BPs-induced secreted sclerostin (SOST), which inhibits the SOST/TGF-β1 signaling to prevent aberrant fibrotic differentiation of rat bone marrow mesenchymal stem cells (BMSCs) and collagen expression, thereby promoting bone formation, remodeling, maturation, and effective mineralization (Fig. 1b).

## Results

### Synthesis and characterization of Mg-ALN

First, magnesium dichloride hexahydrate and alendronate sodium trihydrate were mixed in deionized water using a hydrothermal reaction method and self-assembled to generate a milky-white Mg-ALN under hydrothermal reaction conditions at 120 °C for different reaction times. After washing and drying, Field-emission scanning electron microscopy (FE-SEM) imaging showed that Mg-ALN had a hexagonal rhombic flake morphology independent of the reaction time employed during the synthesis. Statistical analysis revealed that the dimension of the long side of the Mg-ALN size decreased with an increase in reaction time (Supplementary Fig. 1a, b). This is because a short reaction time (<6 h) results in an insufficient yield, affecting Mg-ALN nucleation and generating larger disc sizes (mean length: 13 μm). Conversely, longer reaction times (≥6 h) result in complete reactions, leading to significantly smaller disc sizes (mean length: 4–7 μm). The smallest Mg-ALN were produced with a 24 h reaction time, thus making 24 h the optimal reaction time.

The Mg-ALN synthesized via a 24 h reaction was dispersed in deionized water. After irradiation with a visible light laser pointer, the Tyndall effect was observed, indicating that the Mg-ALN were uniformly dispersed in water under an optical microscope (Fig. 2a and Supplementary Fig. 1c, d). Ultra-high-resolution field-emission transmission electron microscopy (FE-TEM) imaging further confirmed the size and morphology of Mg-ALN (Fig. 2b). Energy dispersive spectroscopy (EDS mapping) and X-ray photoelectron spectroscopy (XPS) qualitative analysis preliminarily confirmed the presence of C, N, O, P, and Mg elements in Mg-ALN, with contents of 37.68 ± 1.56%, 6.85 ± 0.87%, 41.65 ± 0.79%, 11.4 ± 0.87%, and 2.48 ± 0.56%, respectively (Fig. 2c and Supplementary Fig. 1e, f). ImageJ software was used to measure the transverse length of Mg-ALN sizes, resulting in a normal distribution with a median disc size of 3.19 μm (Fig. 2d). Next, the Mg-ALN was analyzed by atomic force microscopy (AFM), revealing a thickness of 11.91 nm (Fig. 2e). The diffraction pattern of Mg-ALN crystals was obtained using an X-ray diffractometer (XRD) and refined using Materials Studio software. The results indicated that Mg-ALN has a monoclinic crystal system, P21/c space group, with $\alpha = \gamma = 90°$, $\beta = 109.75°$, and lattice parameters $a = 12.5892$ Å, $b = 13.6105$ Å, $c = 12.4582$ Å (Fig. 2f). The resulting CIF file was imported into Diamond software to generate the coordination unit and crystal structure images of Mg-ALN (Fig. 2g and Supplementary Fig. 1g–i). Furthermore, we investigated the content of loaded ALN in the Mg-ALN produced by varying the ALN/$MgCl_2$ molar concentration ratio. XRD patterns showed that the peak positions of the Mg-ALN synthesized with different ALN/$MgCl_2$ molar concentrations remained constant, indicating no change in the Mg-ALN crystalline shape (Supplementary Fig. 1j). Interestingly, the highest ALN loading ratio of 53.23 ± 5.8% was observed for Mg-ALN when the ALN/$MgCl_2$ molar concentration ratio (mM:mM) was 2:1. At the same time, it was approximately 38.5 ± 4.3% and 46.7 ± 6.5% for ratios of 1:2 and 1:1, respectively (Fig. 2h). A deionized water solution without Mg-ALN was used for comparative analysis to investigate the neutralization effect of Mg-ALN in a slightly acidic environment. Upon titration with 0.5% hydrochloric acid, it was observed that a deionized aqueous solution containing 5 mg/mL Mg-ALN significantly delayed the decline in pH (Fig. 2i), indicating superior acid neutralization properties.

The biodegradation of Mg-ALN is crucial for potential clinical applications. Therefore, the biodegradability behavior of Mg-ALN was assessed under neutral (pH 7.4) and acidic (pH 6.8 and 4.5) phosphate-

https://doi.org/10.1038/s41467-025-60853-8

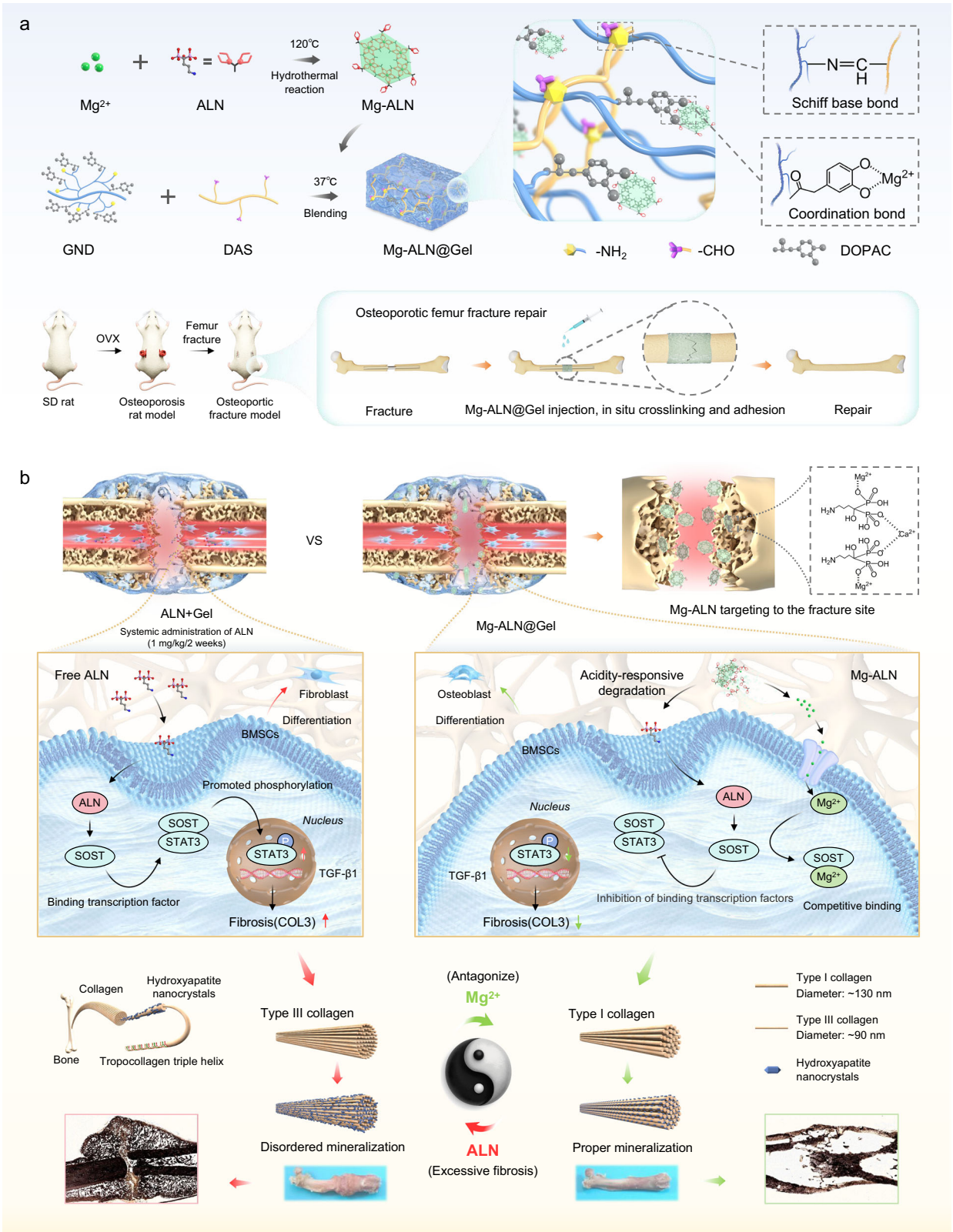


**Fig. 1 | Schematic illustration. a** Magnesium chloride ($MgCl_2$) solution and alendronate sodium (ALN) solution were mixed and subjected to a hydrothermal reaction (120 °C, 24 h) to obtain Mg-ALN, which was then incorporated into catechol- and amine-rich highly branched gelatin/dialdehyde starch networks to synthesise Mg-ALN hydrogel bone adhesive (Mg-ALN@Gel), where $Mg^{2+}$ in Mg-ALN enhanced the cross-linking network of Schiff base-bonded hydrogel. Mg-ALN@Gel was injected locally into a rat model of osteoporotic fracture, and Mg-ALN@Gel responded to the acidic microenvironment of osteoporosis and then degraded through Schiff base bonds, releasing Mg-ALN and promoting osteoporotic fracture repair. **b** Long-term ALN treatment induces the secretion of sclerostin (SOST) in BMSCs and increases the expression of transforming growth factor β (TGF-β) to activate fibroblasts aberrantly. Mg-ALN target the fracture end and acidity-response releases $Mg^{2+}$ and ALN. The $Mg^{2+}$ can competitively bind to SOST and attenuate the SOST/TGF-β signaling pathway, inhibiting fibrogenic differentiation and subsequent disordered mineralization.

https://doi.org/10.1038/s41467-025-60853-8

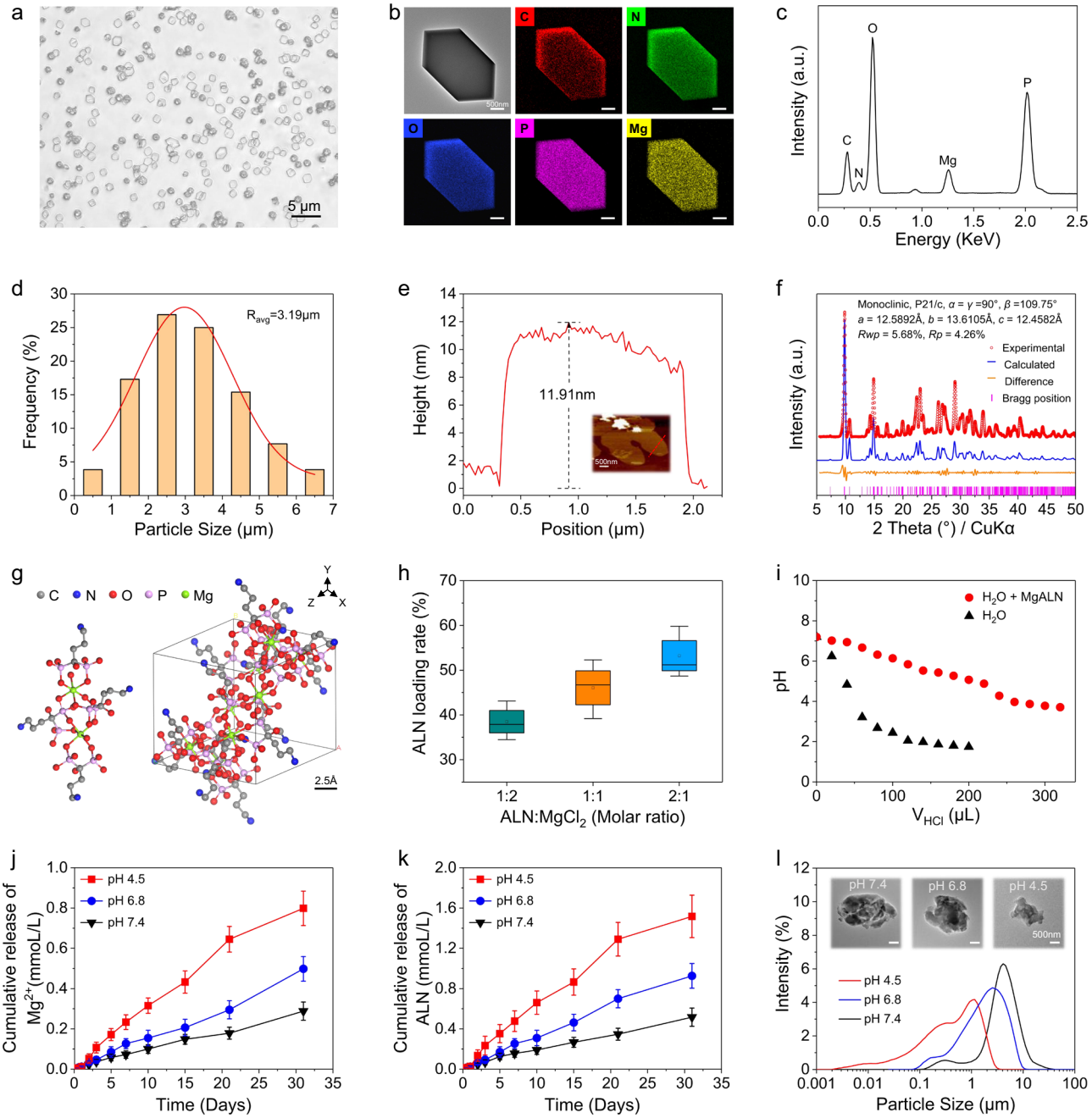


**Fig. 2 | Synthesis and characterization of Mg-ALN. a** Optical microscopy image showing the distribution of Mg-ALN in water, scale bar: 10 μm. **b** TEM images and elemental distribution of Mg-ALN, scale bar: 500 nm. **c** EDS analysis of Mg-ALN. **d** Sizes distribution of Mg-ALN. **e** AFM thickness analysis of Mg-ALN, scale bar: 500 nm. **f** XRD pattern and rietveld refinement results for Mg-ALN. **g** Coordination unit and crystal structure images of Mg-ALN. **h** Drug loading of ALN in Mg-ALN synthesized with different ALN and $Mg^{2+}$ molar ratios, Center lines represent median expressions, the top and bottom edges of the box represent the 75th percentile (upper quartile) and 25th percentile (lower quartile), and whiskers represent the minimal and maximal values ($n = 3$ independent samples). **i** pH changes during the acid-titration experiment with Mg-ALN. $Mg^{2+}$ (**j**) and ALN (**k**) release from Mg-ALN at different time points upon incubation at pH 4.5, 6.8, or 7.4 ($n = 3$ independent samples). **l** The disc size changes of Mg-ALN after incubation for 7 days at pH 4.5, 6.8 or 7.4 were analyzed by laser diffraction and transmission electron microscopy, scale bar: 500 nm. Three independent experiments were performed and representative results are shown in (**a**, **b**, **e**, **l**). Data are presented as mean values ± SEM. Source data are provided as a Source Data file.

buffered saline (PBS) media to simulate healthy (neutral) and osteoporotic (acidic) fluid environments in vivo, respectively. The concentrations of Mg-ALN biodegradation products were measured using a Magnesium Assay Kit and an Alendronate Sodium ELISA Kit (Fig. 2j, k and Supplementary Fig. 1k, l). Initially, we measured the ion or medication content at each time point (0.5, 1, 2, 3, 5, 7, 10, 15, 21, and 31 days) of Mg-ALN incubation under different pH conditions and summed them up. Mg-ALN was released very slowly in PBS at pH 7.4. Still, the release rate significantly accelerates at pH 6.8 and 5.0, indicating the Mg-ALN response to the osteoporotic microenvironment that accelerates the release of $Mg^{2+}$. The release curve of ALN mirrored that of $Mg^{2+}$. Finally, we observed the structural/morphological changes of Mg-ALN after incubation using a laser particle size analyzer (DLS) and transmission electron microscopy (TEM). DLS analysis revealed changes after drying Mg-ALN incubated in different pH environments for 7 days. TEM images showed that the material had degraded at pH 7.4,

with noticeable alterations in morphology and structure. At pH 6.8 and pH 4.5, the Mg-ALN size decreased with decreasing pH, further confirming the acid-responsive degradation and release characteristics of Mg-ALN (Fig. 2l).

### The inhibition of in vitro fibrotic differentiation of BMSCs by Mg-ALN

It is widely acknowledged that bone periosteal stem cells (PDSCs) contribute to osteoblast generation post-bone injury, assume osteoclastic capacity within cartilage, and play a pivotal role in fracture healing[38]. However, in the tissues of BPs-induced AFFs, BMSCs pose a significant impediment to fracture bridging. BPs promote the abnormal differentiation of BMSCs into fibroblasts and, to some extent, hinder the clearance of fibroblast populations. These fibroblasts deposit large amounts of extracellular matrix (ECM) in the fracture space, hindering effective bridging[39,40]. Therefore, the released $Mg^{2+}$ from Mg-ALN is anticipated to inhibit excessive fibrous differentiation of BMSCs, diminish abnormal fibrous tissue, restore bone homeostasis, and foster the healing of BPs-related fractures (Fig. 3a). In a pre-experimental study, we assessed the effects of different concentrations of ALN, $MgCl_2$, and Mg-ALN on fibrotic and osteogenic differentiation of BMSCs and osteoclastic differentiation of mouse bone marrow-derived macrophages (BMDMs) through gene and protein level experiments (Supplementary Figs. 2–4), and the dose–response curves of Mg-ALN were established to guide the optimization of concentration parameters. The results show that Mg-ALN effectively promotes osteogenic differentiation of BMSCs and inhibits osteoclast differentiation in BMDMs within a concentration range of 10–50 μg/mL (Supplementary Fig. 5a, b). Importantly, at 30 μg/mL, Mg-ALN exhibits optimal dual activity: significantly enhancing osteogenesis while suppressing osteoclast formation, along with the lowest induction of fibrotic markers (Supplementary Fig. 5c). These findings suggest that Mg-ALN degradation products exert a favorable, concentration-dependent modulation of the bone remodeling microenvironment, supporting the therapeutic efficacy of the material in promoting bone regeneration while minimizing fibrosis.

Based on these experiments, we selected the optimal ALN, $MgCl_2$, and Mg-ALN concentrations for centralized and re-experimental verification. BMSCs were first induced by a fibrotic differentiation induction solution. After 2 days of induction, media containing ALN (35 ng/mL), $MgCl_2$ (100 μg/mL), and Mg-ALN (30 μg/mL) were replaced and cultured for 1 day. The total RNA was extracted from different groups, and fibrotic genes and anti-fibrotic genes were quantified after reverse transcription and amplification. RT-qPCR results revealed that ALN upregulated the expression of S100 calcium binding protein A4 (*S100a4*), heat shock protein 47 (*HSP47*), and collagen type III alpha 1 chain (*COL3a1*) genes significantly in BMSCs while effectively downregulating the expression of matrix metallopeptidase 8 (*MMP8*) gene. Coordination of ALN with $Mg^{2+}$ to form Mg-ALN effectively downregulated the expression of *S100a4*, *HSP47*, and *COL3a1* genes in BMSCs and upregulated the expression of *MMP8* gene (Fig. 3b). Western analysis detected the protein expression levels of COL3a1 and MMP8 proteins in BMSCs. The ALN group upregulated the expression of COL3a1 protein and downregulated the expression of MMP8 protein. Conversely, $Mg^{2+}$ significantly downregulated the expression of COL3a1 protein and upregulated the expression of MMP8 protein. Compared with the ALN group, the Mg-ALN group also effectively downregulated the expression of COL3a1 protein and upregulated the expression of MMP8 protein (Fig. 3c). Immunofluorescence (IF) staining of COL3a1 and MMP8 further verified that the Mg-ALN group effectively inhibited the fibrotic differentiation of BMSCs. The strongest fluorescence expression of fibrosis and anti-fibrosis was observed in the ALN group, while the $MgCl_2$ group exhibited the weakest anti-fibrosis fluorescence expression but the strongest fibrosis expression. Compared with $MgCl_2$ alone, the anti-fibrosis effect of the Mg-ALN group formed by $Mg^{2+}$ coordination with ALN was weakened, but it still showed a trend similar to that of $Mg^{2+}$ (Fig. 3d, e). In summary, Mg-ALN can inhibit the fibrotic differentiation of BMSCs promoted by ALN through $Mg^{2+}$.

### The promotion of in vitro osteogenic differentiation of BMSCs by Mg-ALN

Homeostasis is maintained by a delicate balance between bone formation by osteoblasts and bone resorption by osteoclasts, and the disruption of this balance in osteoporosis significantly contributes to delayed healing of osteoporotic fractures[41,42]. Ideally, enhancing osteogenic formation and inhibiting osteoclastic activation are conducive to restoring bone homeostasis in osteoporosis. Osteoblasts are mainly differentiated from BMSCs, promoting the directed differentiation of BMSCs into osteoblasts rather than fibrotic cells. Initially, bone alkaline phosphatase (ALP) serves as a phenotypic marker of osteoblasts, directly reflecting the activity or differentiation function of osteoblasts. Alizarin red S (ARS) staining indicates the level of calcium deposition in the extracellular matrix by chelating with calcium ions ($Ca^{2+}$), thereby reflecting the mineralization ability of osteoblasts. BMSCs were induced by an osteogenic induction solution for osteogenic differentiation. After 3 days of induction, media containing ALN (35 ng/mL), $MgCl_2$ (100 μg/mL), and Mg-ALN (30 μg/mL) were replaced for further culture. According to staining images and quantitative analysis, the ALP activity of BMSCs in $MgCl_2$ group and Mg-ALN group were significantly enhanced after 7 days of culture (Fig. 3f, g). After 14 days of culture, more calcium nodules were produced in the $MgCl_2$ and Mg-ALN groups (Fig. 3h, i). Subsequently, we evaluated the expression of osteogenic genes in BMSCs and found that the $MgCl_2$ and Mg-ALN groups significantly upregulated the expression of RUNX family transcription factor 2 (*RUNX2*), osteopontin (*OPN*), osteoprotegerin (*OPG*), and osteocalcin (*OCN*) (Fig. 3j–m). Finally, Osterix (OSX) and OPN protein fluorescence staining were employed to observe the effects of different sample treatments on osteogenic differentiation of BMSCs. The red fluorescence in the upper figure represents nuclear protein IF staining of OSX, while the green fluorescence in the lower figure represents cytoplasmic protein IF staining of OPN. The images show that the BMSCs treated with ALN, $MgCl_2$, and Mg-ALN exhibited positive secretion of OSX and OPN proteins, with fluorescence intensity sequentially enhanced (Fig. 3n, o). These results suggest that the released ALN and $Mg^{2+}$ from Mg-ALN could synergistically promote osteogenic differentiation of BMSCs.

### The inhibition of in vitro osteoclastic differentiation of BMDMs by Mg-ALN

BMDMs were used to verify the osteoclastic inhibition effect of Mg-ALN, as it is a well-studied cell type in osteoclast differentiation. Tartrate-resistant acid phosphatase (TRAP) is a well-recognized indicator of osteoclastic differentiation. The effect of Mg-ALN on the osteoclastic differentiation of BMDMs was assessed through TRAP staining. Under the presence of RANKL-M-CSF or PBS, BMDMs were treated with 100 μg/mL $MgCl_2$, 35 ng/mL ALN, or 30 μg/mL Mg-ALN. Fewer TRAP-positive multinucleated osteoclasts were observed in the ALN group and Mg-ALN group compared to the $MgCl_2$ group (Supplementary Fig. 6a, b). In addition, we evaluated the effect of Mg-ALN treatment on osteoclast bone resorption capacity using a bovine bone resorption assay. BMDMs were seeded onto the surface of bovine bone in the presence of RANKL and M-CSF, and the inhibitory effect of Mg-ALN on osteoclast-mediated bone resorption was assessed. FE-SEM images revealed significant acid-etched bone defects in the $MgCl_2$ group. In contrast, the number and area of bone resorption were reduced significantly in the ALN group and Mg-ALN group (Supplementary Fig. 6c, d). Furthermore, the inhibition of osteoclastic differentiation of BMDMs by Mg-ALN was confirmed through actin and TRAP IF staining. RANKL induction significantly

https://doi.org/10.1038/s41467-025-60853-8

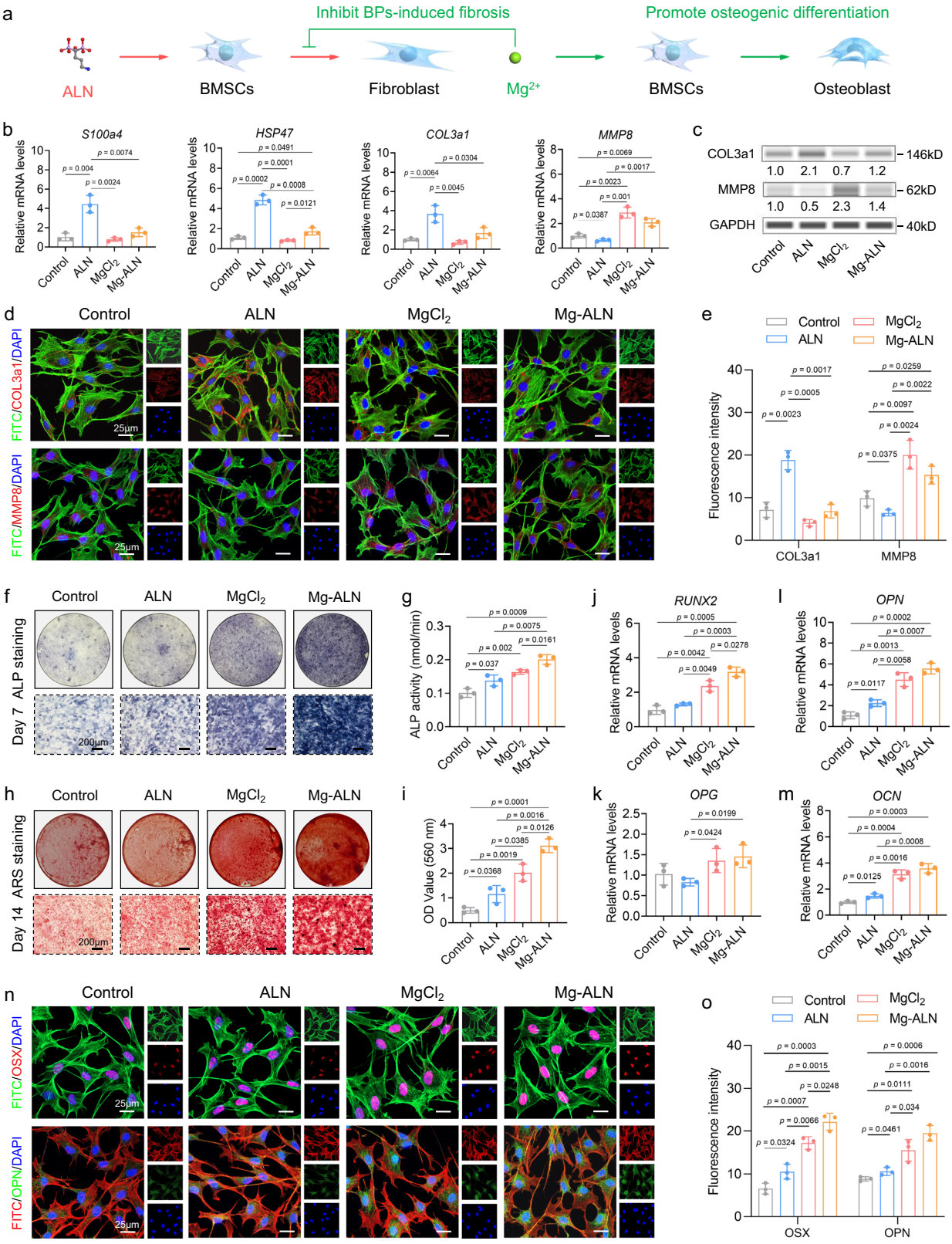


increased the formation of multinucleated osteoclasts from mononuclear macrophages. However, compared to the $MgCl_2$ group, both the ALN group and Mg-ALN group exhibited significant inhibition of multinucleated osteoclast formation (Supplementary Fig. 6e–g). These results indicate that $Mg^{2+}$ did not interfere with the inhibitory effect of ALN on osteoclast activity after ALN coordination to form Mg-ALN.

## Fabrication and characterization of the Mg-ALN@Gel bone adhesive

For the preparation of Mg-ALN@Gel hydrogel, catechol- and amine-rich highly branched gelatin (GND), dialdehyde starch (DAS), and Mg-ALN were synthesized separately. Amine-rich, highly branched gelatin (GN) was obtained from gelatin by halogenation modification. Then a small amount of 3, 4-dihydroxyphenylacetic acid (DOPAC) was used to

**Fig. 3 | In vitro study on the differentiation of BMSCs by Mg-ALN. a** $Mg^{2+}$ inhibits fibrosis of BMSCs associated with BPs and promotes osteogenic differentiation. **b** RT-qPCR analysis of the relative expression levels of fibrosis genes (*S100a4*, *HSP47*, *COL3a1*, and *MMP8*) in BMSCs treated with Mg-ALN ($n = 3$ independent samples). **c** Western blot analysis of the protein expression levels of COL3a1 and MMP8 in BMSCs treated with Mg-ALN, Glyceraldehyde-3-phosphate dehydrogenase (GAPDH) was used as an internal control. **d** Representative image of the staining of fibrosis markers (COL3a1 and MMP8) in BMSCs treated with Mg-ALN, scale bar: 25 μm. **e** Quantitative analysis of COL3a1 and MMP8 fluorescence staining ($n = 3$ independent samples). **f** Representative image of ALP in BMSCs treated with Mg-ALN. **g** Quantitative analysis of ALP staining ($n = 3$ independent samples). **h** Representative image of ARS staining in BMSCs treated with Mg-ALN. **i** Quantitative analysis of ARS staining ($n = 3$ independent samples). **j**–**m** RT-qPCR analysis of the relative expression levels of osteogenic genes (*RUNX2*, *OPN*, *OPG*, and *OCN*) in BMSCs treated with Mg-ALN ($n = 3$ independent samples). **n** Representative image of the staining of osteogenic markers (OSX and OPN) in BMSCs treated with Mg-ALN, scale bar: 25 μm. **o** Quantitative analysis of OSX and OPN fluorescence staining ($n = 3$ independent samples). Three independent experiments were performed and representative results are shown in (**c**, **d**, **f**, **h**, **n**). Data are presented as mean values ± SEM. The significance of differences was assessed using a two-sided Student's *t* test with Tukey's multiple comparison test. Source data are provided as a Source Data file.

amidate GN, replacing part of the amino group on GN and finally synthesizing GND[43] (Supplementary Fig. 7a). As shown in Supplementary Fig. 7b, the results of $^{1}H$ nuclear magnetic resonance (NMR) in a liquid state revealed an increase in the peak intensity at 2.6–2.8 ppm (a, b, c), indicative of the methylene proton of the amine group. In addition, the presence of an amine-ethyl signal at 8.5 ppm (d) suggested the connection of phenol hydroxyl groups in the benzene ring in the GN, confirming the successful synthesis of GND. Furthermore, the introduction of aldehyde groups into starch was achieved through a reaction with sodium periodate, resulting in the oxidation to form dialdehyde starch[44] (Supplementary Fig. 8a). Starch and DAS were characterized using solid-state $^{13}C$ NMR (Supplementary Fig. 8b). The degree of carbonization of C-1 starch shifted to 100.5 ppm, C-2 to 82.05 ppm, C-3, C-4, and C-5 to 72.25 ppm, and C-6 to 61.69 ppm. The NMR spectra of DAS displayed peaks at 100.5, 95.5, 72.25, and 61.69 ppm, corresponding to C-1, C-2, C-5, and C-6, respectively. However, no carbon-based signals were observed in the range of 160–220 ppm, which may be attributed to the existence of hemiacetal groups in DAS. The successful synthesis of DAS was further confirmed by Fourier-transform infrared spectroscopy (FTIR). A unique new peak in the DAS spectrum at 1726 $cm^{-1}$, associated with the carbonyl group (C = O), was detected in comparison to starch, indicating the oxidation of certain hydroxyl groups within the starch. (Supplementary Fig. 8c).

DAS (7% w/v) containing Mg-ALN (30 μg/mL) were combined with GND (30% w/v) at 37 °C, cross-linked via Schiff's base dynamic bonds to form a dual-network Mg-ALN@Gel hydrogel (Fig. 4a). Concurrently, the hydrogel without Mg-ALN was also prepared and named Gel. The internal setting time of the Mg-ALN@Gel hydrogel bone adhesive was determined using a rheological time-sweep test. The gelation point was identified at the crossover of the storage modulus (G′) and loss modulus (G″), indicating the transition from sol to gel state. Based on these measurements, the internal setting time was ~75 s under physiological conditions (37 °C, pH 7.4). This rapid yet controllable gelation process ensures sufficient working time for clinicians to align fracture ends precisely during application, while still achieving stable in situ adhesion. By the same method, the internal setting time of the Gel hydrogel bone adhesive was 95 s (Fig. 4b and Supplementary Fig. 9a). The addition of Mg-ALN notably enhanced the gelation time of the hydrogels, attributed to the formation of coordination bonds between $Mg^{2+}$ sites in Mg-ALN and phenolic hydroxyl groups in DOPAC, facilitating cross-linking. $Mg^{2+}$, acting as an alkaline metal ion, expedited the Schiff's base reaction, thereby accelerating gelation. Moreover, the formation of coordination bonds contributed to enhancing the slow-release effect of Mg-ALN within the hydrogels. Bone tissue repair materials generally need adequate mechanical strength to integrate effectively with the surrounding microenvironment. Rheological measurements indicated that the G′ of both hydrogels exceeded G″ across the entire frequency range, signifying their stability as viscoelastic solids (Fig. 4c and Supplementary Fig. 9b). When Mg-ALN were added, the mechanical properties of Mg-ALN@Gel hydrogels increased significantly, indicating that Mg-ALN promoted the degree of cross-linking of the hydrogels (Supplementary Fig. 9c). Following incubation in PBS, the swelling rates of Gel and Mg-ALN@Gel hydrogel were 485.3 ± 34.6% and 425.1 ± 28.3%, respectively (Supplementary Fig. 9d), the results showed that the addition of Mg-ALN improved the stability of hydrogel and reduced the swelling rate. Additionally, we analyzed the variation in gel viscosity with a shear rate at 37 °C. It was observed that the viscosity of Mg-ALN@Gel hydrogel decreased with increasing shear rate, allowing continuous injection of Mg-ALN@Gel into PBS in its hydrogel state via syringe (Fig. 4d).

Furthermore, hydrogels were injected into molds of various shapes via syringes, yielding stable gels of diverse shapes. These findings suggest that Mg-ALN@Gel hydrogel exhibits favorable injectable and moldable properties (Supplementary Fig. 9e). Schiff's base dynamic bonds confer dynamic properties upon Mg-ALN@Gel hydrogels, enhancing their self-healing capabilities. Strain scanning of the hydrogel at 37 °C revealed that when the strain value reached 100%, the G′ and G″ of the hydrogel remained constant, indicating its ability to withstand a certain degree of elastic deformation (Supplementary Fig. 9f). The healing capability of the hydrogel was illustrated through experiments involving macroscopic visualization. Visual representation of the healing capacity of Mg-ALN@Gel hydrogel post-fracture involved cutting two hydrogel cylinders in half, exchanging and recombining them, followed by incubation at 37 °C for a period (Fig. 4e). Subsequently, the microstructure of the hydrogel was further examined via FE-SEM (Supplementary Fig. 9g). The results showed that the two hydrogel bone adhesives had a three-dimensional network structure, and the pore size of the hydrogels became smaller when Mg-ALN were added, which further indicated that Mg-ALN enhanced the cross-linking density of the hydrogel network. In addition, 3D confocal images demonstrated an uniform distribution of Mg-ALN (red fluorescence) within Mg-ALN@Gel hydrogel (Fig. 4f). Moreover, we assessed the biodegradation behavior of Mg-ALN@Gel in neutral (pH 7.4) and acidic (pH 6.8 and 4.5) PBS media, respectively. The acid-responsive property of Schiff's base bonds in the hydrogels was evident, with degradation rates accelerating progressively with decreasing pH values (Supplementary Fig. 9h). Subsequent evaluation of $Mg^{2+}$ and ALN contents at different time points during Mg-ALN@Gel hydrogel degradation further corroborated the acid-responsive characteristics of Mg-ALN (Fig. 4g, h).

The favorable adhesion and mechanical properties of bone adhesives are crucial for promoting fracture regeneration, especially in cases of comminuted fractures where internal and external fixation of bone fragments is challenging, potentially leading to bone non-unions. Furthermore, effectively filling the space between highly comminuted fragments with complex profiles is essential for satisfactory formation and fixation, promoting effective fracture bridging. To evaluate the adhesive properties of Mg-ALN@Gel bone adhesive, we conducted various tests[29]. Firstly, freshly prepared Mg-ALN@Gel hydrogel was applied between the thumb and index finger of a blue nitrile glove and then firmly adhered to the surface of the glove as the fingers were opened (Fig. 4i). Subsequently, we used Mg-ALN@Gel bone adhesive to splice pig ribs with comminuted fractures (Fig. 4j). Carbon–nitrogen, carbon–sulfur, amino, hydrogen

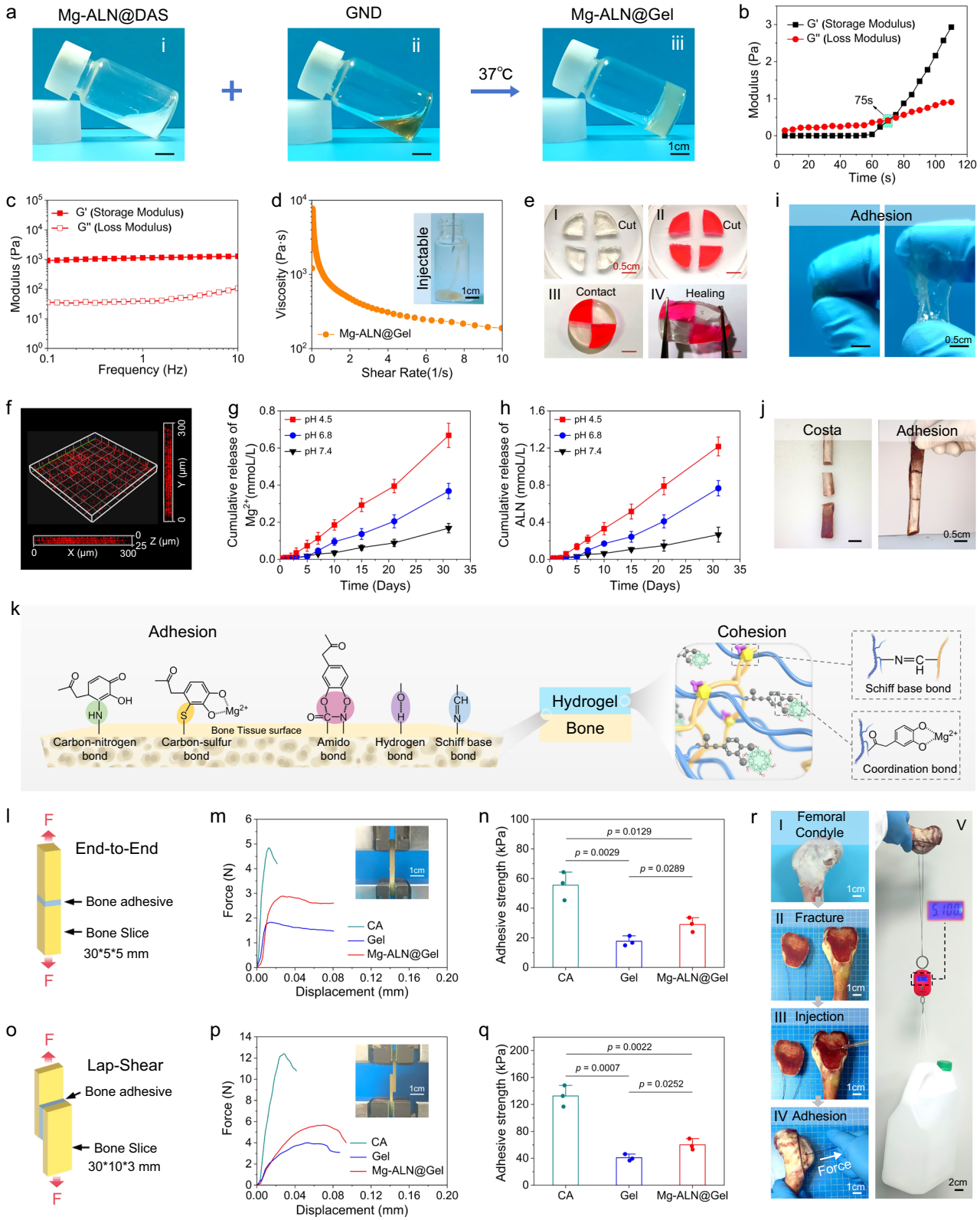


and Schiff base bonds are formed at the the interface between the adhesive and the bone, resulting in the adhesive is allowed to rapidly form an interface adhesion with the bone tissue (Fig. 4k). To assess the mechanical properties of Mg-ALN@Gel bone adhesive, we studied its adhesion strength using bovine femur cortex bone slices. At the same time, adhesive without Mg-ALN (Gel group) and commercial available CA adhesive were also tested for comparative analysis (Fig. 4l, o). Commercial CA adhesive exhibited the highest adhesion strength, with a maximum of 56.9 ± 9.8 kPa in the end-to-end test and 132.6 ± 14.8 kPa in the lap-shear test, indicating robust adhesion (Fig. 4m, n, p, q). Conversely, the Mg-ALN-free adhesive (Gel) displayed the lowest adhesion before adhesion failure. However, the incorporation of Mg-ALN significantly enhanced the adhesion strength of Mg-ALN@Gel, with a maximum of 29.4 ± 3.9 kPa in the end-to-end test and 58.2 ± 7.9 kPa in the lap-shear test. The addition of Mg-ALN increased the crosslink density through coordination

**Fig. 4 | Preparation, characterization and in vitro mechanical properties of the Mg-ALN@Gel bone adhesive. a** Schematic representation of the preparation of the Mg-ALN@Gel bone adhesive. **b** Gelation time of Mg-ALN@Gel. **c** Stability of the Mg-ALN@Gel bone adhesive. **d** Injectability and shear thinning behavior of the adhesive. **e** Self-healing ability of the adhesive. **f** Distribution of Mg-ALN within the adhesive, with red fluorescence representing rhodamine-modified Mg-ALN. The release of $Mg^{2+}$ (**g**) and ALN (**h**) from the Mg-ALN@Gel bone adhesive was measured at different time points after incubation at pH 4.5, 6.8, or 7.4 ($n = 3$ independent samples). **i** Photograph showing strong adherence of the Mg-ALN@Gel bone adhesive to a glove surface. **j** Photograph demonstrating the Mg-ALN@Gel bone adhesive effectively rejoining crushed porcine ribs. **k** Mechanism of adhesion between hydrogel and bone surface and cohesion of internal hydrogel. **l** Schematic representation of end-to-end adhesive strength test setup. **m** Representative force-displacement curve from end-to-end tensile testing. **n** The end-to-end maximum adhesive strength ($n = 3$ independent samples). **o** Schematic representation of lap-shear adhesive strength test setup. **p** Representative force-displacement curve from lap-shear tensile testing. **q** The lap-shear maximum adhesive strength ($n = 3$ independent samples). **r** Photograph depicting strong adherence of the Mg-ALN@Gel bone adhesive to a fragmented femur bone, capable of supporting a bucket filled with 5 L of deionized water. Three independent experiments were performed, and representative results are shown in (**a**, **d**, **e**, **i**, **j**, **m**, **p**, **r**). Data are presented as mean values ± SEM. The significance of differences was assessed using a two-sided Student's *t* test with Tukey's multiple comparison test. Source data are provided as a Source Data file.

bond, enhancing the cohesion of Mg-ALN@Gel bone adhesive (Fig. 4k). To further illustrate the adhesion strength of Mg-ALN@Gel bone adhesive, we re-splinted the condyle part of the pig femur with Mg-ALN@Gel bone adhesive. Subsequently, 5 l of water were poured into the bone, demonstrating the hydrogel's ability to effectively maintain mechanical integrity at the fracture site (Fig. 4r). In addition, we assessed the wet adhesion performance of the Mg-ALN@Gel bone adhesive under biologically relevant conditions. Ex vivo, wet bone fragments were successfully reattached to porcine femurs using the adhesive. After preconditioning in PBS solution under 37 °C to simulate a biological environment, the bonded bone piece capable of sustaining a load of 4.77 kg (Supplementary Fig. 10a). Quantitative lap-shear testing further demonstrated a wet adhesion strength of 49.7 kPa (Supplementary Movie 1 and Supplementary Fig. 10b–d). To better simulate clinical application scenarios, we also evaluated the adhesive under hemorrhagic conditions in vivo using a rabbit tibial comminuted fracture model. Mg-ALN@Gel was injected between bleeding fracture surfaces, where it effectively bonded bone fragments and filled interfacial gaps despite the presence of blood. Notably, its reversible adhesion property enabled real-time repositioning of fragments during surgical alignment (Supplementary Fig. 10e). These findings collectively demonstrate that Mg-ALN@Gel maintains robust adhesive capacity in the presence of blood and other bodily fluids, supporting its feasibility for clinical fracture fixation. This strong wet adhesion is attributed to the catechol and amine functional groups in the gelatin network, which form stable covalent and non-covalent interactions with tissue surfaces even in moist environments.

## Biosafety and bioactivity of Mg-ALN@Gel

As a type of human tissue adhesion material, bone adhesives must meet high standards of biocompatibility. To assess biocompatibility, BMSCs were cultured on top of different adhesives at appropriate concentrations and subjected to live/dead fluorescent labeling. The fluorescent images revealed the majority of cells were viable exhibiting uniform green fluorescence on the surfaces of Gel and Mg-ALN@Gel bone adhesives, indicating healthy cell growth. There were minimal dead cells with red fluorescence in the visual field (Supplementary Fig. 11a). In addition, BMSC proliferation on the surface of different bone adhesives was quantified using a CCK8 assay, showing that BMSC growth on both bone adhesives increased over time, with no significant difference in cell proliferation between the two bone adhesives (Supplementary Fig. 11b). Furthermore, we verified the biological functions of different bone adhesives by quantifying the expression of fibrogenic RNA in BMSCs cultured on Gel and Mg-ALN@Gel bone adhesives using RT-qPCR (Supplementary Fig. 11c–e). The results indicated that compared to Gel, Mg-ALN@Gel significantly reduced the expression of fibrosis genes (*COL3a1* and *S100a4*) and increased the expression of anti-fibrosis genes (*MMP8*). Moreover, we evaluated the effects of Gel and Mg-ALN@Gel bone adhesives on the osteogenic differentiation of surface BMSCs using ALP and ARS quantification. The findings revealed that Mg-ALN@Gel significantly enhanced the osteogenic differentiation of BMSCs compared to Gel alone (Supplementary Fig. 11f, g). Finally, we quantitatively assessed the effects of Gel and Mg-ALN@Gel bone adhesives on the osteoclastic differentiation of surface BMDMs using TRAP staining. In the presence of RANKL and M-CSF, Mg-ALN@Gel significantly inhibited the osteoclastic activation of BMDMs (Supplementary Fig. 11h). These results collectively demonstrate the biocompatibility and biological functions of Mg-ALN@Gel bone adhesive, suggesting its potential as an effective tissue adhesion material for promoting fracture healing.

We administered Cy7-labeled cyanoacrylic adhesives (CA group) and Mg-ALN@Gel bone adhesives subcutaneously into the backs of SD rats, then assessed the biological degradation process in vivo using a small animal imaging system. Over time (1 week, 2 weeks, 4 weeks), the Cy7 signal of Mg-ALN@Gel bone adhesives notably decreased, whereas the Cy7 signal of CA exhibited minimal change (Supplementary Fig. 12a). Skin samples around the adhesive sites were collected and histologically analyzed at 4 weeks. No evident adverse reactions, such as redness or swelling, were observed around the injection sites. Hematoxylin and eosin (HE) staining revealed that the CA group exhibited inflammatory fibrous coating without degradation, while adhesive presence was scarce in the Mg-ALN@Gel group (Supplementary Fig. 12b, c). In addition, adhesive samples were collected and weighed at each time point to further evaluate the degradation rate by percentage of remaining weight (Supplementary Fig. 12d). The systemic toxicity of the adhesive was assessed through histopathological analysis and biochemical blood examination of the heart, liver, kidney, lung, and spleen of rats. No significant accumulation of degradation products or abnormal pathological features was observed in the major organs following implantation of both adhesive groups (Supplementary Fig. 12e). Furthermore, there were no significant changes in total protein (Tp), alanine aminotransferase (ALT), aspartate aminotransferase (AST), and white blood cell (WBC) levels in rats treated with both adhesives compared with the Sham group (Supplementary Fig. 12f), suggesting that neither adhesive caused systemic toxicity. These results indicate that the Mg-ALN@Gel bone adhesive is biodegradable and biocompatible, offering a convenient strategy to accomplish safe auxiliary support for fracture tissue healing.

The longitudinal biosafety profile of various doses of Mg-ALN was subsequently evaluated. Mg-ALN was tested at escalating concentrations (10×, 100×, and 1000×) of its previously determined optimal dose (30 μg/mL). Specifically, Mg-ALN was loaded into 20 μL hydrogel aliquots and administered via dorsal subcutaneous injection to SD rats at concentrations of 300 μg/mL, 3 mg/mL, and 30 mg/mL, corresponding to dose equivalents of 0.02, 0.2, and 2 mg/kg, respectively. The results from both acute toxicity (Day 1) and subacute toxicity (Day 7 and 14) assessments showed that hepatic and renal biomarkers (Supplementary Fig. 13a–d) and blood routine indices (Supplementary Fig. 13e–h) remained within the normal range across all tested doses. This suggests that Mg-ALN maintains good biosafety, even at 1000 times the effective concentration. It is important to highlight that the clinically approved intravenous dose of ALN for osteoporosis is 15 μg/kg/month, while the standard oral dose is 1.16 mg/kg/week[45,46]. For Mg

https://doi.org/10.1038/s41467-025-60853-8

supplementation in osteoporosis, clinical trials have shown efficacy at an oral dose of 1.65 mg/kg/day[47]. The range of doses used in our study (0.02–2 mg/kg) is therefore within a safe therapeutic window, with the Mg-ALN dose of 2 μg/kg in our experiments representing just 13% of the clinical single intravenous ALN dose, 0.17% of the single oral ALN dose, and 0.12% of the single oral Mg dose. This ensures both safety and efficacy.

## Mg-ALN@Gel bone adhesive facilitates osteoporotic fractures repair

The aforementioned experiments demonstrate the potential of Mg-ALN to expedite the healing process of osteoporotic fractures by inhibiting excessive fibrosis and reinstating bone homeostasis. To further validate this hypothesis, an osteoporotic femur fracture model in Sprague-Dawley (SD) rat was established (Fig. 5a), outlining the

**Fig. 5 | Assessment of fixation and healing of an OVX SD rat model of femoral fracture using the Mg-ALN@Gel bone adhesive. a** Experimental design for establishing the OVX SD rat model of femoral fracture and evaluating fracture repair using the Mg-ALN@Gel bone adhesive. **b**, **c** Macroscopic views and MicroCT 3D reconstructed images of healed femurs at 6 and 12 weeks post-treatment with different samples, black scale bar: 1 cm, white scale bar: 2 mm, red scale bar: 500 μm. **d** Quantification of BV/TV, Tb.N, Tb.Pf, Tb.Sp, and SMI at the fracture site after 6 and 12 weeks of treatment with various samples ($n = 3$ biologically independent samples). **e** Safranin O/Fast Green staining at the fracture site after 6 and 12 weeks of treatment with different samples. **f** Quantification of glycosaminoglycan area of Safranin O/Fast Green staining ($n = 3$ biologically independent samples). **g** Picrosirius red staining and polarized light imaging of new bone formation at the fracture site after 6 and 12 weeks of treatment with various samples. **h** Quantification of type I/III collagen ratio ($n = 3$ biologically independent samples). **i** Von Kossa staining of healed femurs at 6 and 12 weeks post-treatment with different samples. Confocal laser scanning microscopy of new bone formation at the fracture site after 6 weeks (**j**) and 12 weeks (**k**) of treatment with various samples. **l** Bone remodeling rate represented by the intensity ratio of calcein green/alizarin red at the fracture site after 6 and 12 weeks of treatment with different samples ($n = 3$ biologically independent samples). **m** The new bone growth speed determined by the distance between calcein green and alizarin red lines ($n = 6$ independent ranges). **n** Four-point bending biomechanical test performed on healed femurs at 12 weeks post-treatment with different samples, with force-displacement curves obtained. The maximum failure load of the healed bone is recorded, the recovery ratio was calculated compared to native femur tissue (**o**), Improvement ratio was calculated compared to the ALN+Gel group (**p**). Three independent experiments were performed and representative results are shown in (**b**, **c**, **e**, **g**, **i**, **j**, **k**, **n**). Data are presented as mean values ± SEM. The significance of differences was assessed using a two-sided Student's *t* test with Tukey's multiple comparison test. Source data are provided as a Source Data file.

experimental design. The femur fracture model was induced following a 12-week period of osteoporosis triggered by ovariectomy (OVX) in female SD rats. To ensure robust experimental outcomes, the animal models were categorized into five treatment groups: Fracture group, CA group, Gel group, ALN+Gel group, and Mg-ALN@Gel group. The Fracture group refers to OVX rats that receive only intramedullary fixation post-femur fracture. In the CA group, the fracture site underwent treatment with clinical cyanoacrylic adhesive after the intramedullary fixation. The Gel group was comprised solely of a pure hydrogel adhesive after an intramedullary fix. The ALN+Gel group involved the systemic administration of ALN (1 mg/kg/2 weeks) in combination with a pure hydrogel adhesive following intramedullary fixation. The Mg-ALN@Gel group involved a hydrogel adhesive loaded with Mg-ALN after an intramedullary fixation.

In order to assess the establishment of an osteoporosis model, three months post-OVX induction in rats (Supplementary Fig. 14a), MicroCT was employed to reconstruct the trabecular structure of the femoral condyle (Supplementary Fig. 14b). The measurements include bone volume fraction (BV/TV), bone density (BMD), trabecular number (Tb.N), and trabecular density (Tb.Sp). In addition, trabecular thickness (Tb.Th) and the SMI index were quantitatively analyzed (Supplementary Fig. 14c). Histomorphological observations were performed on paraffin sections of the distal femur using safranin O staining (Supplementary Fig. 14d). As anticipated, these findings collectively confirmed significant bone loss in cancellous bone among OVX-induced osteoporotic animals, confirming the successful construction of the osteoporosis model in SD rats. Subsequently, OVX rats underwent treatment with a bone adhesive following femur fracture surgery (Supplementary Fig. 15).

Adhesion stability of hydrogel bone adhesive during normal activities is crucial for proper fracture healing. To further validate its stability during movement, we have photographed the motion status of rats injected with the hydrogel at the fracture site and performed gait analysis. The results show that rats in the Fracture group (treated with intramedullary fixation only) exhibited uncoordinated movement of the right hind leg, with the affected limb unable to support weight effectively. In contrast, rats in the Mg-ALN@Gel group (treated with the hydrogel bone adhesive) displayed coordinated movement of both hind legs, demonstrating improved mobility. These observations are presented in Supplementary Fig. 16a–c and Supplementary Movies 2–4. Then, X-ray images taken 6 weeks post-injection revealed poor healing and occasional displacement of the fracture ends in the Fracture group. The Mg-ALN@Gel group showed significantly better healing, with no visible displacement of the fracture ends (Supplementary Fig. 16d–f). While the in vitro metabolism analysis was conducted over a 30-day period, the hydrogel's in vivo performance over 6 weeks can be attributed to several factors: The hydrogel bone adhesive in our study was designed to work in tandem with intramedullary nail fixation to stabilize fracture ends in the initial stage. Even as the material undergoes partial degradation, its breakdown products (including $Mg^{2+}$ and bisphosphonate ligands) continue to exert biological effects such as osteogenesis promotion and fibrosis inhibition. This contributes to sustained functionality even beyond the primary structural phase. The bioadhesive's integration with surrounding bone tissue further stabilizes the fracture interface as healing progresses, reducing the need for continued strong adhesion from the material itself after the initial stages. Therefore, the mechanical stability observed at 6 weeks can be attributed to a dual-phase mechanism: early-stage hydrogel adhesion for initial stabilization, followed by degradation that supports and promotes osteoporotic fracture repair. These findings confirm that the hydrogel bone adhesive can provide sufficient stability to the fracture site during normal activity in rats without the need for external stents.

When combined with the physical map of fracture healing tissue and MicroCT coronal, sagittal, and cross-sectional characterization, along with 3D reconstruction (Fig. 5b, c and Supplementary Fig. 17a, b), it was observed that different fracture tissue samples were incompletely healed at 6 weeks post-healing. Large fibrotic cartilage was evident in the external healing tissue of the fracture, accompanied by an increased callus area. The ALN+Gel group exhibited the largest fibrocartilage. At 12 weeks post-healing, the cyanoacrylate adhesive (CA group) severely impeded bone bridging at the fracture site, proving difficult to guide bone growth and showing even worse outcomes than the fracture group. The Gel adhesive partially promoted fracture healing, as evidenced by the blurred fracture lines. In the ALN administration group (ALN+Gel), abnormal disorganized fibrous bone scabs were accumulated around the fracture site. Conversely, the Mg-ALN@Gel group displayed opaque smooth connections externally. Upon closer inspection, the Mg-ALN@Gel group does not demonstrate perfect healing. Specifically, the coronal, sagittal, and cross-sectional images (Supplementary Fig. 17b) and the 3D reconstructed profile (Fig. 5c) reveal that while significant bone regeneration has occurred, there are still unbridged areas at the fracture site. These results indicate the good effect of Mg-ALN in promoting fracture tissue healing, with a significant reduction in abnormally disorganized fibrous bone scabs compared to the ALN-administered group. Quantitative analysis further confirmed these conclusions (Fig. 5d).

Histologically, the fracture healing effect of different samples was observed through safranin O staining (Fig. 5e, f and Supplementary Fig. 18a). Red indicated fibrocartilage tissue, while green indicated mature bone tissue. Data analysis revealed that at 6 weeks of healing, red fibrocartilage tissue appeared in the fracture spaces of different groups, with the ALN+Gel group exhibiting the highest amount, while the Mg-ALN@Gel group showed the least. By 12 weeks of healing, the red fibrocartilage tissue in the fracture space treated by all sample groups, except the CA group, had disappeared, suggesting that the CA adhesive severely impeded osteogenic activity around the fracture site and delayed fracture bridging. Abnormal accumulation of

disorganized fibrous bone scabs was observed around the fracture in the ALN+Gel group. In contrast, the Mg-ALN@Gel group displayed a higher proportion of mature lamellar bone tissue. These results indicate that Gel-based bone adhesives-assisted fracture fixation positively impacted fracture healing. Importantly, the released $Mg^{2+}$ from Mg-ALN could inhibit the fibrosis of fracture tissue promoted by ALN. Goldner's trichrome staining was employed to further assess the fracture healing effect of different sample treatments, and the results were in line with safranin O staining (Supplementary Fig. 18b). TRAP staining was utilized to observe the anti-osteoclast effect of the various treatments. Red staining represented positive osteoclasts (Supplementary Fig. 18c). The findings indicated that at 6 weeks, a substantial number of red-positive osteoclasts were observed at the fracture site of the Fracture group, CA group, and Gel group, while no red osteoclasts were present in the ALN+Gel group and Mg-ALN@Gel group. These results suggested that ALN combined with $Mg^{2+}$ generate Mg-ALN able to inhibit osteoclast activation. Polarized light images of collagen fibers revealed the presence of red type I collagen and green type III collagen in the healed fracture tissues at 6 and 12 weeks. Among these, the systemic administration group of ALN exhibited the highest number of type III collagen fibers with a relatively disordered arrangement, potentially leading to excessive fibrosis within the fracture tissue space (Fig. 5g, h). Von Kossa staining was utilized to assess the distribution and content of calcium nodules in the tissue, reflecting the mineralization capacity of the fracture-healing tissue. Abnormal fibrosis in the ALN+Gel group ultimately leads to disordered mineral deposition on collagen fibrils (Fig. 5i and Supplementary Fig. 19a). Effective bone regeneration requires the orderly growth of hydroxyapatite in type I collagen, which promotes moderate mineralization and scab maturation. However, systemic administration of ALN (ALN +Gel group) induces tissue fibrosis and produces excess type III collagen. As type III collagen has a finer diameter than type I collagen (~90 nm for type III collagen, ~130 nm for type I collagen), its increased specific surface area allows an increase in the number of hydroxyapatite nanocrystal binding sites, leading to disordered mineral deposition during the late healing phase, resulting in a decrease in the mechanical properties of bone tissue[48]. In the Mg-ALN@Gel group, type I collagen was arranged orderly under polarized light and exhibited normal mineralizing ability in Von Kossa staining, yielding mature lamellar cortical bone that was observed at 12 weeks of healing. In conclusion, the released $Mg^{2+}$ from Mg-ALN can inhibit the growth of BPs-induced excessive type III collagen, the formation of disorganized fibrous bone scabs and abnormal mineralization and promote fracture tissue healing. In addition, the dual labeling of calcein/alizarin red was employed to assess the bone remodeling rate, with the fluorescence intensity ratio serving as the indicator. The distance between calcein and alizarin denotes the rate of new bone formation, with a greater distance indicating a faster rate of new bone formation (Fig. 5j–m). After 6 weeks of healing, the Fracture group, CA group, and Gel group exhibited a relatively low rate of bone remodeling and formation. In contrast, the ALN+Gel group and Mg-ALN@Gel group demonstrated relatively higher rates. These findings suggest that $Mg^{2+}$ and ALN exhibit significant effects in promoting bone formation. Furthermore, quantitative analysis of the distances revealed that the bone formation rate in the Mg-ALN@Gel group was higher than in the ALN+Gel group, potentially attributed to the sustained-release effect of Mg-ALN. Analysis at 12 weeks of healing indicated a notable decrease in bone remodeling and formation rates in the Mg-ALN@Gel group, signifying the formation of more mature lamellar bone tissue compared to other groups. Finally, the four-point biomechanical test showed that the maximum failure load of the Mg-ALN@Gel group was significantly higher than that of both the Gel group and the ALN+Gel group (Fig. 5n and Supplementary Fig. 19b). Conversely, samples treated in the CA group exhibited a lower maximum load compared to the Fracture group, reflecting its adverse role in the healing process likely due to poor biocompatibility and biodegradability. The experimental group (Mg-ALN@Gel) showed a 107.4% increase in flexural strength compared to the Fracture group (Supplementary Fig. 19c). Compared to other work (refs. 35,36,37), the flexural strength of Mg-ALN@Gel bone adhesive promotes osteoporotic fracture healing through inhibition of fibrosis and improvement in disordered mineral deposition, significantly outperforming most of the previous studies (Supplementary Fig. 19d)[35–37]. Notably, the experimental group (Mg-ALN@Gel) recovered 90.8% of the flexural strength compared to native femur and showed a 27.8% improvement over the ALN+Gel group (Fig. 5o, p).

## $Mg^{2+}$ inhibits the SOST/TGF-β1 signaling to prevent excessive fibrosis

Due to the superior therapeutic effects of Mg-ALN both in vivo and in vitro, we performed an analysis of the transcriptomes of fracture tissues from the Gel group, ALN+Gel group, and Mg-ALN@Gel group, using RNA sequencing methods, aiming to elucidate the underlying biological mechanisms. Initially, principal component analysis (PCA) revealed variability among the three groups with no correlation with each other (Supplementary Fig. 20a), and there were differentially expressed genes (DEGs) among the three groups (Supplementary Fig. 20b). Subsequently, we examined the DEGs through the heat map between ALN+Gel group and Gel group (ALN+Gel vs Gel), as well as between Mg-ALN@Gel group and ALN+Gel group (Mg-ALN@Gel vs ALN+Gel). The horizontal axis denotes the magnitude of difference between the two groups, where a larger absolute value indicates a greater disparity in gene expression. The vertical axis represents the corrected *P* value, with a higher value indicating increased significance. Gray dots signify non-DEGs, while blue and red dots denote DEGs, with blue indicating upregulated genes and red indicating downregulated genes (Fig. 6a, b). The top ten upregulated genes and top ten downregulated genes in ALN+Gel vs Gel and Mg-ALN@Gel vs ALN+Gel were selected by *P* value and log2 (FoldChange) comprehensive sequencing, respectively. This analysis allowed us to narrow down the potential key genes for further study. As shown in Supplementary Fig. 20c–e, the two datasets uniquely converge at SOST. This overlap highlights its critical role in the observed differential expression patterns, indicating that SOST is a key target for investigating the effects of Mg-ALN@Gel on fibrosis and bone healing. In addition, previous studies have demonstrated that elevated sclerostin (encoded by the *SOST* gene) levels are associated with impaired fracture healing[49,50]. Furthermore, we constructed protein interaction networks (PPIs) using the STRING database, which revealed that SOST was linked to TGF-β1, a pivotal protein involved in fibrosis (Fig. 6c). In addition, TGF-β1 was found to be associated with fibrosis markers such as COL3a1, as well as anti-fibrosis indicators including MMP8 and matrix metallopeptidase 23 (MMP23). We additionally confirmed the influence of Mg-ALN on the protein levels of SOST and TGF-β1 in BMSCs through western analysis. (Fig. 6d). The results showed that ALN significantly promoted the expression of SOST and TGF-β1 in BMSCs, while $MgCl_2$ and Mg-ALN significantly inhibited their expression. This indicates that $Mg^{2+}$ inhibited the ALN-induced promotion of SOST and TGF-β1 expression.

Next, we used HDOCK software to simulate the protein-protein docking between SOST protein and signal transducer and activator of transcription 3 (STAT3, TGF-β1 transcription factor)[51]. The results indicated that the amino acids of STAT3 could be successfully docked into the pocket of SOST, forming a 21-hydrogen-bonded linkage with a binding force of −1230.1 kcal/mol, signifying a robust binding interaction between SOST protein and STAT3 (Fig. 6e, f and Supplementary Fig. 21). Furthermore, docking simulations of $Mg^{2+}$ to the SOST protein pocket demonstrated a highly stable binding (Fig. 6g). SOST activity decreased (Fig. 6d) after Mg binding to the active site of SOST, which may be due to covalent modification or metal ion binding induced protein inactivation[52,53]. Notably, immunoprecipitation experiments revealed that $MgCl_2$ treatment prevented the precipitation of anti-

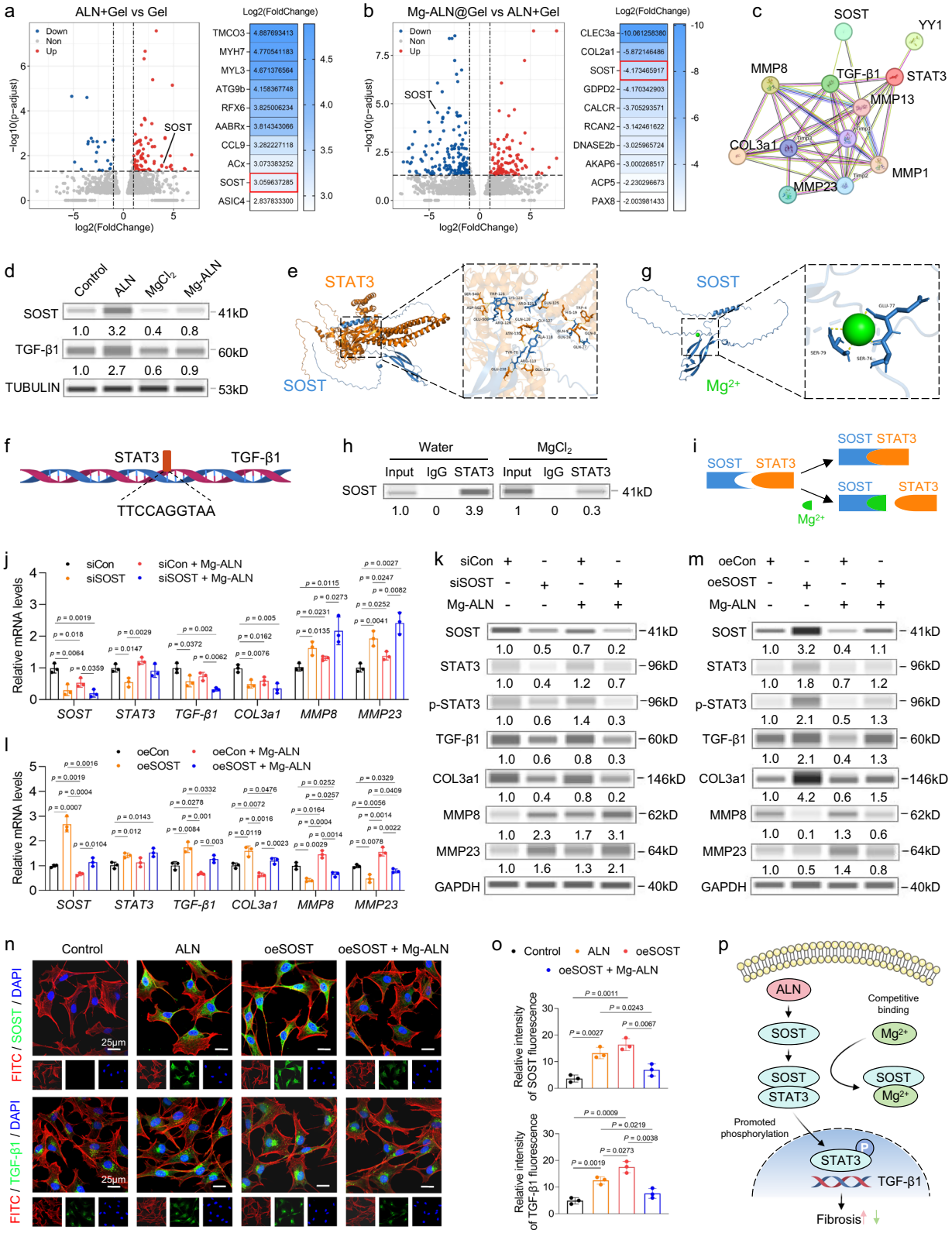


STAT3 by SOST (Fig. 6h), possibly due to disruption of their interaction through blocking the pocket on SOST (Fig. 6i). In addition, the docking of $Ca^{2+}$ and SOST protein was simulated. No hydrogen bonding was observed during the docking process (Supplementary Fig. 22a). Immunoprecipitation experiments showed that $CaCl_2$ treatment did not prevent SOST from interacting with anti-STAT3 antibodies (Supplementary Fig. 22b). The above indicated that $Ca^{2+}$ does not share the same functionality as $Mg^{2+}$ in this context. Based on the above experiments, we hypothesized that $Mg^{2+}$ inhibits fibrosis by suppressing the SOST/TGF-β1 signaling pathway in BMSCs cells. We further investigated whether SOST silencing or overexpression would alter the expression of fibrosis-associated factors in BMSCs cells at both the gene and protein levels. Our findings demonstrated that SOST silencing led to the upregulation of anti-fibrotic indicators MMP8 and MMP23, accompanied by downregulation of STAT3, phosphorylated STAT3 (p-STAT3), TGF-β, and the fibrotic indicator COL3a1 in BMSCs,

**Fig. 6 | $Mg^{2+}$ prevent aberrant fibrotic differentiation by inhibiting the SOST/TGF-β1 signaling pathway in BMSCs. a** Volcano plots of DEGs for ALN+Gel vs Gel, on the right side of the volcano map are the top ten upregulated genes by *P* value and log2 (FoldChange) comprehensive sequencing. **b** Volcano plots of DEGs for Mg-ALN@Gel vs ALN+Gel, on the right side of the volcano map are the top ten downregulated genes by *P* value and log2 (FoldChange) comprehensive sequencing. Gray: non-DEGs; red: upregulated DEGs; blue: downregulated DEGs. **c** Protein interaction networks of DEGs. **d** Western blot analysis of SOST and TGF-β1 expression in BMSCs, TUBULIN was used as an internal control. **e** Protein-protein interaction interface of SOST and STAT3. **f** Mapping of potential STAT3 binding sites in TGF-β1 transcription factor predicted by rVista 2.0 software. **g** Docking of $Mg^{2+}$ with the SOST pocket. **h** Co-immunoprecipitation showing $Mg^{2+}$ inhibition of SOST-STAT3 binding in BMSCs. **i** Scheme depicting $Mg^{2+}$ blocking SOST-STAT3 interaction. **j** The relative RNA expression levels of *SOST*, *STAT3*, *TGF-β1*, *COL3a1*, *MMP8*, and *MMP23* in BMSCs with SOST knockout (n = 3 independent samples). **k** The protein expression levels of SOST, STAT3, TGF-β1, COL3a1, MMP8, and MMP23 in BMSCs with SOST knockout, GAPDH was used as an internal control. **l** The relative RNA expression levels of *SOST*, *STAT3*, *TGF-β1*, *COL3a1*, *MMP8*, and *MMP23* in BMSCs with SOST overexpression ($n = 3$ independent samples). **m** The protein expression levels of SOST, STAT3, TGF-β1, COL3a1, MMP8, and MMP23 in BMSCs with SOST overexpression, GAPDH was used as an internal control. **n** IF staining representative image of SOST and STAT3 protein expression in BMSCs overexpressing SOST treated with Mg-ALN. **o** Quantitative analysis of SOST and STAT3 fluorescence staining ($n = 3$ independent samples). **p** Schematic diagram of $Mg^{2+}$ inhibition of the SOST/TGF-β1 signaling pathway. Three independent experiments were performed and representative results are shown in (**d**, **e**, **g**, **h**, **k**, **m**, **n**). Data are presented as mean values ± SEM. The significance of differences was assessed using a two-sided Student's *t* test with Tukey's multiple comparison test. Source data are provided as a Source Data file.

with a more pronounced effect observed following the addition of Mg-ALN (Fig. 6j, k). Conversely, overexpression of SOST in BMSCs resulted in significant downregulation of anti-fibrotic indicators MMP8 and MMP23, while STAT3, p-STAT3, TGF-β1, and COL3a1 were markedly upregulated. Furthermore, STAT3, p-STAT3, TGF-β1, and COL3a1 proteins were significantly downregulated, and MMP8 and MMP23 proteins were markedly reduced in samples with the addition of Mg-ALN following SOST overexpression compared to SOST overexpression alone (Fig. 6l, m).

In addition, the impact of Mg-ALN on the secretion of SOST and TGF-β1 proteins from BMSCs was further examined via IF staining. The cytoskeleton is visualized in red, the nucleus in blue, and SOST and TGF-β1 in green fluorescence. Analysis of the figures reveals that untreated BMSCs secrete minimal amounts of SOST and TGF-β1 proteins. Following ALN treatment, cells exhibited a significant increase in the secretion of SOST and TGF-β1 proteins. SOST-overexpressing BMSCs displayed fluorescence intensity comparable to that of the ALN group. Interestingly, the secretion of SOST protein was markedly inhibited by Mg-ALN treatment in SOST-overexpressing BMSCs, which was attributed to the release of $Mg^{2+}$ from the Mg-ALN complex. The $Mg^{2+}$ ions bind to the active site of SOST, leading to a decrease in SOST expression (Fig. 6n, o). Based on the aforementioned experiments, we deduce that ALN enhances SOST expression in BMSCs. Subsequently, SOST binds to the STAT3 protein, a transcription factor for TGF-β1, thereby promoting the phosphorylation of STAT3. Phosphorylated STAT3 then binds to TGF-β1, thereby up-regulating TFG-β1 expression and consequently promoting the expression of fibrosis-associated factors. Upon release of $Mg^{2+}$, its competes for binding to SOST-STAT3, leading to the dissociation of STAT3. Consequently, this impedes the promotion of STAT3 phosphorylation and attenuates the expression of ALN-induced fibrosis factors (Fig. 6p). In summary, the released $Mg^{2+}$ from Mg-ALN curtails excessive fibrotic differentiation of BMSCs cells by downregulating SOST/TGF-β1 signaling, thereby potentially expediting the healing process of BPs-related fractures.

To further validate that the released $Mg^{2+}$ from Mg-ALN promote osteoporotic fractures healing by antagonizing the ALN-induced excessive fibrosis through the SOST/TGF-β1 pathway. Fracture healing is a complex cascade process, and the quality of fracture healing was reflected by studying fibrosis-associated protein expression under different stages (Fig. 7a). In this regard, we analyzed the fracture healing tissues of the Gel group, ALN+Gel group, and Mg-ALN@Gel group by immunohistochemical (IHC) staining and IF staining. The IF images were captured using the same exposure time, as well as identical detector gain settings across all samples and color channels. This ensures consistency in image capture and allows for valid comparisons of fluorescence intensity. By staining results and quantitative analysis, there was a high differential expression of SOST (red arrows) in the ALN+Gel group compared to the other groups from 6 to 12 weeks postoperatively (Fig. 7b, c). IF staining was performed on fracture tissue at different healing times (6 and 12 weeks) using dipeptidyl peptidase 4 (CD26) antibodies (Supplementary Fig. 23a–d). The results showed that the fluorescence intensity of CD26 was the strongest in ALN+Gel group, suggesting that the excessive fibrosis induced by BPs was associated with CD26-positive fibroblasts in this study. Next, we performed IF staining for STAT3, TGF-β1, MMP23 and COL3a1 proteins on fracture healing tissues with different healing times. The results showed that from 6 weeks (Fig. 7d–k) to 12 weeks (Fig. 7l–s), the ALN systemically administered group had the most pronounced fluorescence of STAT3 and TGF-β1 expression relative to the other groups, the highest fluorescence intensity of fibrotic COL3a1 protein, and the weakest fluorescence intensity of anti-fibrotic MMP23 protein. The quantitative results also showed that there was a differential expression in the ALN+Gel group relative to the other groups. It indicates that the Mg-ALN formed by the coordination of $Mg^{2+}$ and ALN in the experimental group are delivered locally. On the one hand, Mg-ALN is released sustainably in response to acids in vivo, so that only a small amount of medication concentration is required to achieve the medication effect and reduce the toxic side effects. On the other hand, $Mg^{2+}$ inhibits excessive fibrosis by downregulating SOST/TGF-β1 signaling, thus promoting more efficient bridging of osteoporotic fractures.

## Discussion

BPs, acting as organic counterparts to inorganic pyrophosphates, stand as the primary pharmacological agents in clinical practice for managing conditions related to low bone mass. These encompass osteoporosis, bone fractures, Paget's disease, bone cancers, and bone metastases to bone from various primary cancers (such as prostate, lung, and breast cancers), among others[54]. The therapeutic effectiveness of BPs relies on their specific affinity for the P-C-P bond in bone tissue. Upon entering the bloodstream, BPs preferentially bind to sites of active bone remodeling during resorption, impeding the valproic acid pathway in osteoclasts and ultimately disrupting their function. Several BPs have been approved for treating osteoporotic symptoms, including alendronate, zoledronate, risedronate, and ibandronate. In 2005, Odvina et al. first reported nine patients with spontaneous nonvertebral fractures following prolonged (3–8 years) BPs treatment, six of whom experienced delayed fracture healing or non-union despite clinical intervention[55]. Subsequently, there has been a growing body of clinical evidence linking BPs to specific types of femoral fractures. The American Society for Bone and Mineral Research (ASBMR) classifies and terms this pathology as AFFs, typically involving sub-trochanteric or diaphyseal regions and associated with non-traumatic or low-energy trauma. Biopsy findings from most AFFs patients reveal a marked deficiency in osteoblast number and activity, alongside reduced osteoclast function[56]. Moreover, the absence of new bone formation observed through tetracycline labeling indicates inhibited bone formation within the fracture gap of AFFs[57].

https://doi.org/10.1038/s41467-025-60853-8

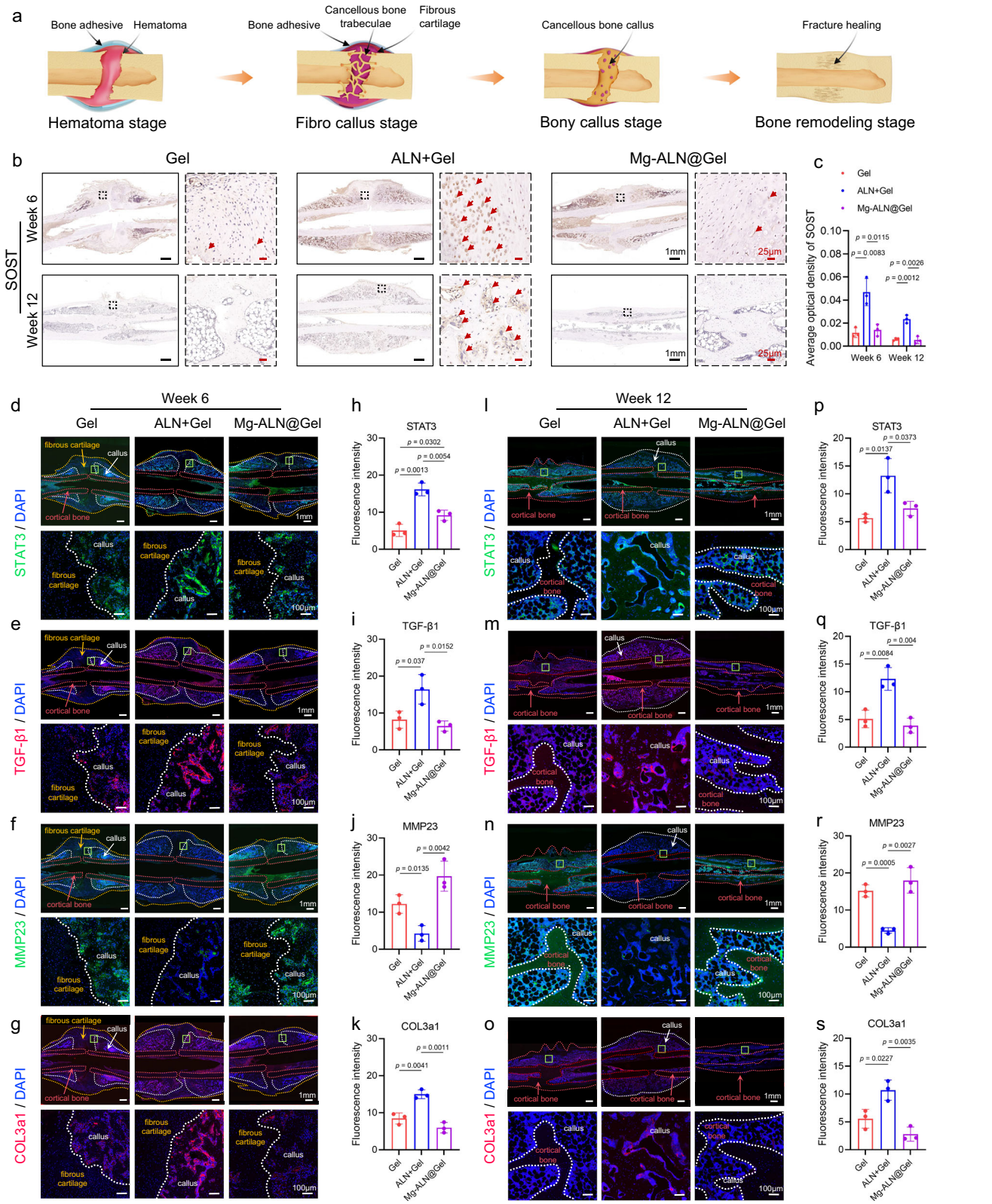


Zheng et al. have elucidated that BPs could redirect the differentiation pathway of BMSCs towards specific fibroblast clusters through single-cell sequencing (scRNA-seq). This redirection results in abnormal accumulation and inadequate clearance of the ECM, culminating in the formation of excessive fibrosis. This aberrant fibrotic tissue not only impedes subsequent osteogenic differentiation but also creates an unfavorable microenvironment for the repair of AFFs, ultimately compromising the structural integrity of bone tissue[17].

Fracture healing is a dynamic and complex process consisting of four consecutive and overlapping stages: hematoma stage, fibrocallus stage, bony callus stage, and bone remodeling stage (Fig. 7a). A recent study suggests that the key pathological feature of delayed fracture healing induced by BPs is the excessive formation of fibrotic tissue, which interferes with the bridging of the external bone scab. This outcome is primarily associated with excessive fibrosis during the second phase of fracture healing. Consequently, addressing the

**Fig. 7 | $Mg^{2+}$ inhibit the SOST/TGF-β1 signaling to prevent excessive fibrosis.** **a** Four consecutive and overlapping stages of fracture healing: hematoma stage, fibrocallus stage, bony callus stage, and bone remodeling stage. **b** Representative images of SOST protein immunohistochemical staining at 6 and 12 weeks after femur fracture repair with Gel, ALN+Gel, and Mg-ALN@Gel treatments, nuclei were stained blue or purple, and SOST target proteins were stained brown in the cytoplasm, black scale bar: 1 mm, red scale bar: 25 μm. **c** Quantitative analysis of SOST protein immunohistochemical staining ($n = 3$ biologically independent samples). Representative images (**d**–**g**) of STAT3, TGF-β1, MMP23, and COL3a1 protein IF staining at 6 weeks post-repair. Quantitative analysis (**h**–**k**) of STAT3, TGF-β1, MMP23, and COL3a1 protein IF staining at 6 weeks post-repair ($n = 3$ biologically independent samples). Representative images (**i**–**o**) of STAT3, TGF-β1, MMP23, and COL3a1 protein IF staining at 12 weeks post-repair. Quantitative analysis (**p**–**s**) of STAT3, TGF-β1, MMP23, and COL3a1 protein IF staining at 12 weeks post-repair ($n = 3$ biologically independent samples). Three independent experiments were performed and representative results are shown in (**b**, **d**, **e**, **f**, **g**, **l**, **m**, **n**, **o**). Data are presented as mean values ± SEM. The significance of differences was assessed using a two-sided Student's *t* test with Tukey's multiple comparison test. Source data are provided as a Source Data file.

adverse effects of increased BPs-induced excessive fibrosis and promotion of proper mineralization is essential to improve osteoporotic fractures repair.

Mg can increase bone mass and promote bone healing mainly by activating osteoblast differentiation and adhesion, as well as promoting the migration and adhesion of human bone-derived cells. Indeed, Mg has been recognized for its critical role in bone metabolism, particularly its capacity to inhibit bone resorption[58,59]. In addition to counteracting bisphosphonate (BP)-induced fibrosis, Mg contributes directly to bone metabolism by regulating the balance between bone resorption and formation. This dual functionality ensures the therapeutic efficacy of the Mg-ALN MOF system, mitigating adverse effects while promoting effective fracture healing under osteoporotic conditions. The incorporation of Mg into the system leverages these synergistic effects to optimize outcomes. Based on this, a self-sacrificing Mg-ALN material is synthesized, which is formed by the coordination of ALN and $Mg^{2+}$. Mg-ALN aims to neutralize the acidic microenvironment and release $Mg^{2+}$ and ALN in response to environmental triggers. It is widely acknowledged that PDSCs are pivotal in generating osteoblasts following bone injury, enabling endochondral osteogenic capabilities, and contributing significantly to fracture healing[38]. However, in the context of tissues affected by BPs-induced AFFs, BMSCs assume a central role in impeding fracture bridging. BPs induce the aberrant differentiation of BMSCs into fibroblasts and obstruct the removal of fibroblast populations, resulting in the deposition of substantial amounts of ECM within the fracture gap, thereby impeding its bridging. In vitro experiments conducted in this study demonstrated that $Mg^{2+}$ could curb the excessive fibroblastic differentiation of BMSCs, foster their osteogenic differentiation, and bolster the bone formation process. Furthermore, ALN was observed to mitigate mature osteoclast-mediated bone erosion by inhibiting osteoblastic activation of BMDMs, thereby attenuating mature osteoclast-mediated bone erosion.

The experimental findings were further corroborated in a rat model of osteoporotic femur fracture, where the systemic administration of the ALN group (ALN+Gel) replicated the pathological features of AFFs. The healing efficacy and underlying mechanism were observed and explored through comparative analysis. To enhance the efficacy of Mg-ALN while minimizing toxic side effects, local biomaterial delivery to accomplish fracture site fixation represents an optimal strategy for achieving improved healing outcomes[60,61]. To deliver on this, we developed an injectable hydrogel bone adhesive (Mg-ALN@Gel) cross-linked using Schiff's base dynamic bonds. This cross-linking mechanism increases the degree of adhesive cross-linking and enhances its cohesion by chelating $Mg^{2+}$ from Mg-ALN through the phenolic hydroxyl groups of catechol. The Mg-ALN@Gel hydrogel exhibits good biocompatibility, predictable degradation rate, adjustable mechanical strength, injectability, and tissue adhesion. On the one hand, the Mg-ALN@Gel was designed to fix the fracture ends with the assistance of intramedullary nail fixation. This fixation facilitates gait coordination and creates mechanical stimulation at the fracture site that promotes fracture repair. Bone growth and development are indeed mechanosensitive processes, and the role of mechanical loading in fracture healing is well established. The adaptation of bone to mechanical loading, as originally described by Wolff's law, continues to influence bone remodeling during fracture healing[62]. In our study, we acknowledge that during the early stages of fracture healing, BMSCs are subject to low-magnitude mechanical stimulation. This stimulation promotes their proliferation and chondrogenic differentiation, contributing to the formation of cartilaginous tissue bridges[63]. As healing progresses, these mechanical cues also regulate the expression of osteogenic and osteoclastic genes, contributing to the remodeling of the cartilaginous callus into a mineralized bone callus, primarily through the dynamic equilibrium between OPG and RANKL signaling[64]. While gait coordination generates mechanical stimuli at the fracture site, potentially enhancing healing, the primary focus of this study is on the role of the Mg-ALN@Gel bone adhesive in preventing excessive fibrosis to facilitate osteoporotic fracture repair. On the other hand, the Mg-ALN@Gel not only provides fracture stabilization but also serves as a carrier for the controlled release of $Mg^{2+}$ and ALN in response to the osteoporosis-associated acidic microenvironment. Animal experiments have demonstrated that ALN can inhibit osteoclast activation, thereby exerting anti-resorptive effects. However, ALN adversely induces fibrosis at the fracture healing site, which leads to excessive production of type III collagen. Which increases its specific surface area due to its finer diameter than type I collagen, leading to disordered mineral deposition in the later stages of healing, resulting in a decrease in the mechanical properties of the bone tissue[48]. Proper heterotopic ossification stabilizes the fracture ends and promotes healing[65–67]. However, in this study, abnormal heterotopic ossification was observed in the ALN+Gel group compared to the Gel group. This abnormality can be attributed to excessive fibrosis induced by the long-term systemic administration of ALN (a bisphosphonate medication). The fibrosis led to abnormal mineralization, which ultimately resulted in significant ectopic bone tissue growth and callus formation. Addressing these side effects of ALN-induced fibrosis was a primary focus of this study. On the side, $Mg^{2+}$ inhibits the growth of type III collagen, facilitates the migration and differentiation of chondrocytes, and then promotes the osteogenic differentiation of BMSCs. Consequently, the Mg-ALN increases the ratio of type I/III collagen, improves disordered mineral deposition on collagen fibrils, reduces production of disorganised fibrous bone scabs, ultimately improve mechanical strength properties of healing bone tissue and effective bridging of fractures.

In the realm of current research on tissue fibrosis mechanisms, the TGF-β signaling pathway undeniably assumes a pivotal role in fibrosis pathogenesis. Pathologically, TGF-β overexpression induces epithelial–mesenchymal transition (EMT), ECM deposition, among other processes, culminating in fibrotic disorders. Given the paramount significance of TGF-β and its upstream and downstream molecules in fibrosis progression, inhibiting the TGF-β signaling pathway emerges as a promising therapeutic strategy for fibrotic tissue treatment[16]. Fan et al. illustrated that TGF-β1 exerts an anti-hepatic fibrotic effect through ECM1 protein downregulation[68]. Szeto et al. demonstrated that verteporfin, an effective YAP inhibitor, ameliorates renal fibrosis by suppressing the YAP/TAZ pathway, which consequently downregulates TGF-β[69]. Hence, we postulate that SOST, linked to TGF-β1, exhibits significant differential expression in ALN+Gel vs Gel

and Mg-ALN@Gel vs ALN+Gel, as deduced from transcriptome sequencing and protein interactions enrichment analysis. Previous studies suggest that SOST acts as a bone formation inhibitor and is a potential target for osteoporosis treatment. SOST inhibits bone formation by hindering the Wnt signaling pathway and by suppressing the bone morphogenetic protein (BMP) signaling pathway. This is achieved through binding to the Wnt co-receptor or low-density lipoprotein receptor 5 (LRP5) and LRP6. Downregulating the SOST gene proves advantageous in enhancing bone mass and reducing bone resorption[70]. Conversely, Liu et al. unveiled a subset of hepatic focal nodular hyperplasia (FNH)-specific endothelial cells expressing SOST uniquely through multilevel bioinformatics analysis and experimental validation, which could have robust interaction with fibroblasts and foster liver fibrosis via the PDGFB/PDGFRB pathway[71]. In our study, we delve deeper into understanding how SOST impacts TGF-β1 expression. Protein-protein interfaces (PPIs) are indispensable for biological processes, including fibrogenesis and progression. These interactions rely heavily on key residues, and disruptions may occur due to the presence of additional ions or small molecules. Through molecular docking and immunoprecipitation experiments, we demonstrated that $Mg^{2+}$ antagonizes the ALN-induced excessive fibrosis by disrupting SOST-STAT3 binding and inhibiting STAT3 phosphorylation.

In conclusion, the injectable hydrogel adhesion platform developed in conjunction with Mg-ALN exhibited rapid and fibrosis-preventing osteoporotic fractures healing, inhibiting excessive fibrosis and restoring dysfunctional bone homeostasis. Our findings highlight that self-sacrificing Mg-ALN can successfully promote acid-responsive release of $Mg^{2+}$ and address the adverse effects of BPs-induced excessive fibrosis by suppressing the SOST/TGF-β1 signaling pathway in BMSCs. It increases the ratio of type I/III collagen and promotes osteogenic differentiation of BMSCs, proper mineralization and maturation of the callus. Ultimately, the Mg-ALN@Gel hydrogel bone adhesive promotes effective bridging of osteoporotic fractures, with a 28.9% improvement in flexural strength over the control group after 12 weeks of treatment. This work provides a potential therapeutic approach and elucidates mechanisms for anti-bone fibrosis.

## Methods

### Ethical statement

All animal experiments were conducted in accordance with the guidelines approved by the ethics committee of the Institutional Animal Care and Use Committee at South China Agricultural University, with ethics review numbers 2023D005 and 2023D021.

### Materials

Magnesium chloride hexahydrate ($MgCl_2 \cdot 6H_2O$, AR, >99%, Aladdin, China), Alendronate sodium trihydrate (ALN, 97%, Aladdin, China). Gelatin (V900863, Merck, Germany); 2-chlorethylamine hydrochloride (C107599, aladdin, China); Hydrochloric acid (H399657, Aladdin, China); 1-ethyl-(3-dimethylaminopropyl) carbamide diimide (EDC, E106172, aladdin, China); N-hydroxythiosuccinimide (Sulfo-NHS, H109337, aladdin, China); 3, 4-dihydroxyphenylacetic acid (D106475, aladdin, China); Starch from maize (aladdin, A120984); Sodium periodate (S104091, aladdin, China); Rhodamine B (R104960, Aladdin, China); Low-glucose dulbecco's modified eagle's medium (DMEM), α-minimum essential medium (α-MEM), fetal bovine serum (FBS), penicillin–streptomycin, trypsin and phosphate-buffered saline (PBS) were obtained from Gibco (USA); Dexamethasone (≥97%, D4902, Merck, Germany); Ascorbic acid (A4403, Merck, Germany); Sodium β-glycerophosphate (G9422, Merck, Germany); L-proline (P5607, Merck, Germany); Trisodium L-ascorbate-2-phosphate salt (49752, Merck, Germany); bFGF (HY-P7091, MedChemExpress, USA); Alizarin Red S (A5533, Merck, Germany); Sodium phosphate (S113693, Aladdin, China); Hexadecylpyridinium chloride (C129534, Aladdin, China); Recombinant mouse M-CSF protein (416-ML, R&D Systems, USA); Recombinant mouse TRANCE/RANKL/TNFSF11 (*E. coli*-expressed, 462-TEC, R&D Systems, USA); Bovine Serum Albumin (BSA, A1933, Merck, Germany) Calcein (C0875, Merck, Germany); Alizarin 3-methyl-aminodiacetic acid (A3882, Merck, Germany).

### Preparation of Mg-ALN

$MgCl_2 \cdot 6H_2O$ (40 mM, 25 mL) and ALN (40 mM, 25 mL, 40 °C) were dissolved in deionized water to clarify the solutions, respectively. Then, slowly add the $MgCl_2 \cdot 6H_2O$ solution to the ALN solution and stir continuously until the solution becomes milky-white. Afterward, place the mixture in a hydrothermal reactor and react at 120°C for 1, 6, 12, and 24 h. After the reaction, centrifuge to collect the precipitate and wash it with ultra-pure water three times before drying it in an oven (45 °C) for future use.

### Characterization of Mg-ALN

The dispersion of Mg-ALN in water was observed by optical microscopy (IX83, Olympus, Japan). The morphologies of Mg-ALN were characterized using Field emission by high-resolution transmission electron microscopy (FE-TEM, Thermo Scientific Talos F200S G2S/TEM, USA) and Field-emission scanning and electron microscopy (FE-SEM, Zeiss Sigma 300, Germany). The distribution of chemical elements of the Mg-ALN was detected by Energy Dispersive Spectroscopy (EDS, Thermo Scientific Talos F200S G2S/TEM, USA). The thickness of Mg-ALN was measured by atomic force microscopy (AFM, Dimension Edge, Bruker, Germany). The crystal structure of the Mg-ALN was detected by X-ray diffraction (XRD, Smartlab 9KW, Rigaku, Japan). The XRD pattern was refined using Materials Studio software (MS 2019) to simulate the crystal structure of Mg-ALN and obtain a crystallographic information file (CIF). The crystal structure map of Mg-ALN was drawn by Diamond 4.6 software. The elemental composition and chemical state of the sample surface were analyzed by X-ray photoelectron spectroscopy (XPS, ESCALAB 250Xi, Thermo Fisher Scientific, USA).

### Neutralization titration experiment

Mg-ALN (5 mg/mL) was incubated and stirred in deionized water before the dropwise addition of 0.5% hydrochloric acid. The pH level was constantly observed with a pH meter, and titration was deemed complete once the pH fell below 1 for three consecutive measurements.

### pH-triggered $Mg^{2+}$ and ALN release of Mg-ALN

A total of 100 mg of Mg-ALN was introduced into 2 mL of PBS buffer at pH levels of 7.4, 6.8, and 4.5, respectively. Following incubation at 37 °C for different time points (0.5, 1, 2, 3, 5, 7, 10, 15, 21 and 31 days), the released $Mg^{2+}$ and ALN were collected in an EP tube and then analyzed by a microplate reader (Bio-Rad, USA) following the Magnesium Assay Kit (Nanjing Jiancheng Bioengineering Institute) and Alendronate Sodium ELISA Kit (Shanghai Lianmai Biological Engineering Co., LTD). The morphology of Mg-ALN following treatment with various pH buffers was examined using FE-TEM. At the same time, the respective disc size of Mg-ALN was measured by a laser particle size analyzer (DLS, BT-9300LD, Dandongbaite, China).

### Loading efficiency

The content of ALN in the total input system was recorded as Wm, and the content of ALN in the supernatant obtained by centrifugation after the hydrothermal reaction was recorded as We. The drug loading of ALN was obtained as a weight percentage according to the formula (Wm − We)/Wm × 100%.

### Preparation of amine-rich, highly branched gelatin (gelatin-$NH_2$, GN)

In total, 9 g gelatin was dissolved in 90 mL PBS at 40 °C, and 10.5 g 2-chlorethylamine hydrochloride was added to the 90 mL PBS

solution. Then, 90 mL 1 M sodium hydroxide (NaOH) aqueous solution was added and stirred at 40 °C for 24 h. The solution was neutralized with 1 M hydrochloric acid (HCl) to a pH value of 7.0-7.2, prior to dialysis was performed in deionized water for 3 days, whereby the dialysis solution was replaced with fresh DI every 6–8 h. The product, namely Gelatin-$NH_2$ (GN), was isolated via freeze-drying and stored in a dryer.

### Preparation of catechol- and amine-rich highly branched gelatin (gelatin-$NH_2$-DOPAC, GND)

In all, 1 g Gel-$NH_2$ was dissolved in 100 mL of 2×PBS (pH 6) solution in a round-bottom flask under heat and magnetic stirring until the Gel was completely dissolved. 1-ethyl -(3-dimethylaminopropyl) carbamyl diimide (EDC, 0.5 g) and N-hydroxythiosuccinimide (Sulfo-NHS, 0.575 g) were dissolved in 2 mL 2×PBS (pH 6) buffer solution respectively, and then slowly added dropwide to the above mixture by drop. Following 5-min reaction under magnetic stirring, 100 mg of 3, 4-dihydroxyphenylacetic acid (DOPAC, 10%) was dissolved in 5 mL dimethyl sulfoxide (DMSO) solution. After dissolution, the mixture was added to the above solution and stirred at 40 °C for 24 h. The pH of the mixture was maintained at 5–6. Dialysis in pure water (pH 4–5) was carried out for 3 days, replacing the dialysate every 6–8 h. The product, namely, Gelatin-$NH_2$-DOPAC (GND), was collected by freeze-drying and stored in a dryer, until further use.

### Preparation of dialdehyde starch (DAS)

In all, 5 g of starch was dispersed in 50 mL of deionized water at 37 °C. A 7.5% w/v solution of sodium periodate (50 mL) was gradually incorporated into the mixture, which was then allowed to react in the dark for 12 h. Following the reaction, the product was rinsed with deionized water, and the pH was adjusted to 7.0. It was then freeze-dried and stored in a dryer and designated as DAS.

### Characterization of GND and DAS

Liquid-state $^1$H nuclear magnetic resonance (NMR) spectroscopy was applied to analyze the physical and chemical properties of Gelatin, GN and GND.

Solid-state $^{13}$C NMR spectroscopy (Avance Neo 400WB, Bruker, Germany) was applied to analyze the physical and chemical properties of the starch and DAS. The functional groups of the starch and DAS were identified by Fourier-transform infrared spectroscopy (FTIR, TENSOR27, Bruker, Germany).

### Preparation of Mg-ALN@Gel

In brief, the DAS dry powder was dissolved in PBS to form a solution (7% w/v), and then, the Mg-ALN (30 μg/mL) was added into the DAS solution and dispersed ultrasonic for 10 min. Moreover, the gelatin (30% w/v) was dissolved in PBS. After that, the DAS/Mg-ALN mixture was combined with the gelatin solution in a 1:1 volume ratio and mixed uniformly at 37°C to create Mg-ALN@Gel hydrogel.

### Characterization of Mg-ALN@Gel

The performance of the Mg-ALN@Gel injection is observed and photographed when the Mg-ALN@Gel is injected into 37 °C water. The three-dimensional porous structure of the hydrogel surface was observed by FE-SEM after freeze-drying.

The addition of 1 mM of rhodamine B during the synthesis of Mg-ALN as described above was carried out to prepare a hydrogel containing rhodamine B-modified Mg-ALN. The distribution of red fluorescence was observed by laser confocal microscopy. The excitation wavelength is 555 nm, and the emission wavelength is 580 nm.

To verify the self-healing properties of Mg-ALN@Gel, two identical gel discs (ø: 16 mm, h: 5 mm) were prepared, one stained with red ink. The discs were then cut into four equal pieces and recombined, followed by incubation at 37 °C for 5 min. A tweezer was used to hold the ends of the healed gel and pull it symmetrically, aiming to observe and capture its self-healing ability.

### Rheological analysis

A Rheometer (Physica MCR301, Anton Paar, Austria) was employed for the rheological evaluation. The gelation time of the bone adhesive was assessed by monitoring the storage modulus (G′) and loss modulus (G″) following the initiation of gelation. The mechanical properties of the bone adhesive were determined using a rheometer in frequency sweep mode from 0.1 to 10 Hz with a strain amplitude of 1.0%. The injectability of the bone adhesive was characterized by measuring the linear viscosity (η) in frequency sweep mode. The critical strain point of the hydrogel was detected via strain amplitude sweeps (γ = 0.01–1500%).

### Characterization of adhesive and mechanical properties in Mg-ALN@Gel hydrogel

The adhesivity of Mg-ALN@Gel hydrogel bone adhesive was demonstrated by qualitative tests, whereby the hydrogel was used to join fractured ribs and femurs. The joint femur was then anchored to a rope pulling a water bottle.

Other than the above qualitative tests, quantitative tensile measurements were also performed, whereby the force-displacement curves and maximum adhesive strengths of Mg-ALN@Gel hydrogel bone adhesive were recorded in both end-to-end and lap-shear configurations.

To evaluate the wet adhesion capability of the Mg-ALN@Gel hydrogel bone adhesive under hematic conditions, a comminuted tibial fracture model was established in New Zealand white rabbits (female, 6-month-old, 3 kg ± 0.25 kg). Briefly, the animals were anesthetized, and a longitudinal skin incision was made over the tibial region, followed by dissection through the underlying fascia and periosteum. A complete osteotomy was performed at the mid-shaft of the tibia using an electric saw, and the bone was randomly fragmented into four pieces. The fracture fragments were then reduced and stabilized using the Mg-ALN@Gel hydrogel bone adhesive at the fracture site.

### Swelling behavior

The swelling rate of hydrogel was assessed using the gravimetric method. The cross-linked products' weight ($W_1$) was measured prior to 120-h soaking in PBS to obtain the wet sample weight ($W_t$). The swelling ratio was calculated using the formula: $[W_t\text{-}W_1)/W_1]\times100\%$.

### In vitro degradation

The initial weight (W1) of the hydrogel was weighed and incubated in PBS with different pH values (7.4, 6.8, and 4.5) at 37 °C. After drying, the remaining hydrogel weight ($W_t$) was recorded at different time points (3, 6, 9, 12, 15, 18, 21, 24, 27, and 29 days). The weight remaining was calculated to evaluate the degradation behavior of the hydrogel according to the formula: Wt/W1 × 100%. The supernatant was collected (0.5, 1, 2, 3, 5, 7, 10, 15, 21 and 31 days) in an EP tube and then analyzed by a microplate reader (Bio-Rad, USA) following the Magnesium Assay Kit (Nanjing Jiancheng Bioengineering Institute) and Alendronate Sodium ELISA Kit (Shanghai Lianmai Biological Engineering Co., LTD).

### Cells and animals

Rat bone marrow mesenchymal stem cells (BMSCs) were purchased from Shanghai Cell Bank, Chinese Academy of Sciences. BMSCs were cultured in low-glucose DMEM containing 10% FBS and 1% penicillin–streptomycin. Bone marrow-derived macrophages (BMDMs) from mice were isolated in the lab. In summary, 6-week-old female C57BL/6 mice (18 g ± 2 g) were sourced from the Laboratory Animal Management Center at Southern Medical University in China.

The blood of the femoral and tibia-pulp cavities were washed into α-MEM medium containing 10% FBS and 1% penicillin–streptomycin, then blown and mixed, filtered through a screen, and then centrifuged (100 × *g*, 3 min). To obtain pure BMDMs, the cells were finally dispersed into the above medium containing 50 ng/mL M-CSF. Following a culture period, it can be used in cell experiments.

Female Sprague-Dawley (SD) rats, New Zealand white rabbits, and C57BL/6 mice were sourced from the Laboratory Animal Management Center at Southern Medical University in China. All animals were housed under a 12/12-h light/dark cycle with controlled environmental conditions (temperature: 20–26 °C; humidity: 50–60%). Throughout the experiment, the animals had ad libitum access to food and water.

### Fibrogenic differentiation

BMSCs with appropriate cell density were inoculated into culture plates, and the cell culture medium was replaced with fibrous induction culture medium (10 nM dexamethasone, 50 ng/mL ascorbic acid and 10 mM sodium β-glycerophosphate).

### Osteogenic differentiation

BMSCs with appropriate cell density were inoculated into culture plates, and the cell culture medium was replaced with osteogenic induction culture medium (10 nM dexamethasone, 50 ng/mL ascorbic acid and 10 mM sodium β-glycerophosphate).

### Osteoclast differentiation

BMDMs with appropriate cell density were seeded into culture plates, and the cell culture medium was replaced with osteoclastogenic induction culture medium (50 ng/mL M-CSF and 50 ng/mL RANKL).

### Alkaline phosphatase (ALP) staining assay

After 7 days of osteogenic differentiation, BMSCs were fixed using 4% paraformaldehyde and subsequently stained with a BCIP/NBT Alkaline Phosphatase (ALP) Colorimetric Kit (C3206, Beyotime, China). Following this, an Alkaline Phosphatase Assay Kit (P0321S, Beyotime, China) was employed to assess ALP activity quantitatively.

### Alizarin red S (ARS) staining assay

BMSCs were cultured for 14 days after osteogenic induction, prior to 10-min staining with 2% Alizarin Red S (ARS, pH 8.3), followed by washing with ultra-pure water and image acquisition. Quantitative analysis was further performed to assess the degree of mineralization in different treatment groups, where calcium nodules were dissolved in a sodium phosphate (0.01 mol/L) solution containing 10% hexadecylpyridinium chloride before measuring the absorbance at 570 nm.

### Tartrate-resistant acid phosphatase (TRAP) staining and quantification

Following 7 days of osteoclast differentiation, BMDMs were fixed with 4% paraformaldehyde and stained with a Tartrate-resistant Acid Phosphatase (TRAP) Stain Kit (G1492, Solarbio, China). A Tartrate-resistant Acid Phosphatase Test Kit (P0332, Beyotime, China) was utilized to assess TRAP activity quantitatively.

### Bone slice resorption assay

BMDMs were inoculated on beef bone slices using α-MEM containing recombinant RANKL and M-CSF. The medium was changed regularly. After 10 days, the bone slices were then rinsed with a solution of sodium hypochlorite bleach. Finally, FE-SEM and ImageJ software were used to image samples and quantify the area ratio of bone resorption.

### Transduction

To obtain BMSCs knocking down SOST (siSOST), the BMSCs were inoculated in 6-well plates at an appropriate density with low-glucose DMEM medium containing FBS. When the cells were 60–70% confluence, the serum-free low-glucose DMEM was followed by the sequential addition of 8 μL/mL interferon (Polyplus) and 50 nM of SOST siRNA oligonucleotide (RIBOBIO, China) transfection reagent. In addition, 50 nM of nucleotides (RIBOBIO, China) was used as a control. After transfection for 24 h, low-glucose DMEM containing FBS was replaced to continue incubation for 24 h. RT-qPCR was used to verify the expression of the *SOST* gene.

To obtain BMSCs overexpressing SOST (oeSOST), the BMSCs were inoculated in 6-well plates at an appropriate density with low-glucose DMEM medium containing FBS. When the cells were 60–70% fused, the serum-free low-glucose DMEM was followed by the addition of 8 μL/mL of interferon (Polyplus) and 10 μL of lentivirus-packed SOST cDNA ($1 \times 10^8$ TU/mL) sequentially. In addition, 10 μL of empty cloning vector ($1 \times 10^8$ TU/mL) lentivirus was added as a control group. After 24 h, low-glucose DMEM containing FBS with 0.3 mg/ml puromycin (Sigma) was added to continue the culture, and the cells were screened and survived. After 7 days, *SOST* overexpression was confirmed by RT-qPCR.

### Gene expression

Total RNA was isolated from cells using the SimplyP RNA Extraction Kit (BSC52M1, BioFlux). Reverse transcription was conducted using the ToloScript All-in-one RT EasyMix for qPCR Kit (22107-01, TOLOBIO) to transcribe RNA into cDNA. For real-time quantitative PCR (RT-qPCR), the primers (Supplementary Table 1) and the 480 SYBR Green fluorescent dye (22204-01, TOLOBIO) were added, and cDNA was amplified using the Real-time quantitative polymerase chain reaction (RT-qPCR) system. β-ACTIN was used as an internal control gene, and the relative expression level of the target gene was calculated using the $2^{-\Delta\Delta Ct}$ method.

### Western (WES) analysis

Cellular protein samples were obtained using RIPA (Radio Immunoprecipitation Assay) lysis buffer (P0013B, Beyotime, China), and the protein concentration was determined using a BCA Protein Concentration Determination Kit (P0010, Beyotime, China) to ensure that it met the requirements for electrophoresis. Next, the automated Western blotting system (WES™ system, ProteinSimple, Bio-Techne, USA) and WES Separation Kit (SM-W004-112-230, kDa Jess/Wes Separation Module, 8 × 25 capillary cartridges) were used for the electrophoretic separation of target proteins (The primary antibody concentration for the target protein is listed in Supplementary Table 2). Finally, the relative quantity of each protein was measured by the area under the peak in chemiluminescence. Uncropped and unprocessed scans of the most important blots were provided in the Source Data file.

### Immunoprecipitation (IP) test

After incubating BMSCs with 100 μg/mL $MgCl_2$ for 3 days, the cells were lysed using RIPA lysis solution, followed by incubation at 4 °C for 30 min. The cells were then centrifuged (18,000 × *g*, 4 °C, 30 min) and the supernatant was collected. Next, the supernatant was incubated overnight with STAT3 antibody and isotype control antibody at 4 °C under shaking conditions. Overall, 10 μL of pre-treated Protein A agarose beads were added to the overnight cell lysate and slowly shaken at 4 °C for 2–4 h to bind the STAT3 antibody to the Protein A agarose beads. The mixture was then centrifuged (860 × *g*, 4 °C, 3 min) and the supernatant was discarded. Next, the agarose beads were washed with lysis buffer, and 15 μL of 2×SDS sample buffer was added, and the protein was denatured and quantified. Finally, western analysis was performed together with an anti-SOST antibody.

### Immunofluorescence (IF) staining

After fixing the cells with 4% formaldehyde at room temperature for 30 min, the membranes were permeabilized with PBS containing 0.1%

Triton X-100, followed by blocking with PBS containing 1% BSA at room temperature for 2 h. Then, the primary antibody (Supplementary Table 3) was incubated overnight at 4 °C. After washing, the secondary antibody was incubated at room temperature. Thereafter, the cells were stained with FITC for the cytoskeleton and DAPI for the nucleus, and images were acquired using a high-resolution confocal laser scanning microscope (CLSM, Zeiss, LSM 800 With Airscan, Germany). Quantitative analysis was performed using the ImageJ software.

### In vivo degradation and biological toxicity assessment

In all, 200 mL of Cy7-labeled (0.1 mM) cyanoacrylate adhesive (CA) and Mg-ALN@Gel adhesive (the concentration of Mg-ALN was 30 μg/mL) were injected into the dorsal regions of SD rats, respectively. The degradation of the hydrogel was monitored at different time points (0 week, 2 weeks, 4 weeks) using a small animal live optical imaging system (PerkinElmer, IVIS Lumina HTX, USA). The adhesive was collected and weighed at each time point to further quantify the extent of adhesive degradation as a percentage of the remaining weight. After 4 weeks, the rats were sacrificed, and the skin tissue surrounding the different adhesives was fixed in 4% formaldehyde, followed by paraffin embedding and hematoxylin–eosin (HE) staining. The skin was further evaluated for biodegradability. The heart, liver, spleen, lungs, and kidneys were used to assess the in vivo toxicity of different bone adhesives.

To longitudinally evaluate the biosafety of Mg-ALN, the compound was tested at escalating concentrations (10×, 100×, and 1000×) relative to its optimal dose (30 μg/mL). Specifically, Mg-ALN was loaded into 20 μL hydrogel aliquots and administered via dorsal subcutaneous injection to SD rats at concentrations of 300 μg/mL, 3 mg/mL, and 30 mg/mL, corresponding to doses of 0.02, 0.2, and 2 mg/kg, respectively. Finally, the acute toxicity (Day 1) and subacute toxicity (Days 7 and 14) of Mg-ALN were evaluated by detecting hepatic and renal biomarkers and blood routine indices.

### Osteoporotic femur fracture model

Osteoporosis was induced by bilateral ovariectomy of female SD rats (6-week-old, 200 g ± 20 g). Twelve weeks later, the osteoporotic rats had their right femurs subjected to mid-shaft transverse osteotomy and were stabilized with an intramedullary K-wire (ø: 1.2 mm). Mg-ALN@Gel bone adhesive was injected around both ends of the osteotomized site. Thirty rats were randomly divided into five groups and two time points (6 and 12 weeks): Fracture, CA, Gel, ALN+gel, and Mg-ALN@Gel. Rats were euthanized at 6 and 12 weeks post-surgery for further testing.

### MicroCT and analysis

The healing fracture samples collected at 6 and 12 weeks were fixed in 70% alcohol for 3 days. Samples were subsequently scanned using a MicroCT system (Bruker, SkyScan 1276) with an X-ray source voltage of 85 kV, a current of 200 μA, a 1 mm aluminum filter to optimize contrast, an exposure time of 460 ms, a rotation step length of 0.4°, and a resolution of 15 μm. Using DataViewer software, different views (coronal, sagittal, axial) were observed, while CTvox was used for three-dimensional reconstruction, and the CTAn software was used to quantitatively analyze the area located 3 mm above and 3 mm below the fracture position. Quantitative indicators included the bone volume fraction (BV/TV), bone density (BMD), trabecular number (Tb.N), trabecular separation (Tb.Sp), trabecular thickness (Tb.Th), and SMI index.

### Histological evaluations

To assess bone mineralization, calcein (20 mg/kg) was injected inTRAPeritoneally 10 days before sacrifice, and Alizarin 3-methylamino-diacetic acid (30 mg/kg) was given inTRAPeritoneally 3 days prior. After imaging, the bone samples were fixed in 70% ethanol, dehydrated with alcohol and acetone, and embedded in methyl methacrylate solution. The femur was sliced into 5-μm sections, which were subsequently examined using a CLSM (Zeiss, LSM 800 with Airscan, Germany), and images were captured for further analysis. Next, the sliced samples were stained with Von Kossa and imaged under an optical microscope (Olympus). Finally, the images were analyzed using ImageJ software to determine the rate of mineralization.

To observe the healing effects of fracture tissue and explore their mechanisms, the collected specimens were fixed in 4% paraformaldehyde and then decalcified for 21 days. From each specimen, 3-mm slices were cut and embedded in paraffin. For the evaluation of femoral fractures, Safranin O/Fast Green staining, Sirius scarlet staining, Goldner's trichrome staining, and TRAP staining were used. The tissue sections stained with Sirius scarlet were observed by a polarized light microscope (Leica, DM4P, Germany) and the images were obtained. Other stained tissue sections were scanned using a digital pathology scanner (3D-histech, PANNORAMIC, Hungary). Immunohistochemical (IHC) staining and bone tissue immunofluorescence (IF) staining were performed with antibodies against SOST, STAT3, TGF-β1, COL3a1, and MMP8 (Supplementary Tables 4 and 5).

### Four-point biomechanical bending test

To assess the biomechanical properties of the healing tissue in osteoporotic fractures, four-point bending tests were conducted using an electronic universal testing machine (Hegewald & Peschke, Germany). Briefly, the femoral samples were placed between two horizontal platforms of the bending device, which were maintained at a fixed distance apart. The loading speed was kept constant at 1 mm/min until the bone tissue failed completely, and the maximum load at failure was recorded.

### mRNA sequencing (RNA-seq)

RNA samples are isolated from in vivo fracture healing tissues containing Gel, ALN+Gel, and Mg-ALN@Gel, and submitted to Novogene Co., Ltd. for whole transcriptome analysis.

### Molecular modeling and docking

First, the structure of the target protein was predicted by Uniprot and the PDB file was obtained. Next, ClusPro was used for protein docking, and the model with the highest score was selected and imported into PDBePISA to calculate the binding energy.

### Statistics and reproducibility

Data are presented as mean ± standard deviation (SD). Two-sided Student's $t$ test with Tukey's multiple comparison test were used to compare the results among different groups. Results were considered statistically significant if $P < 0.05$. Each experiment was repeated a minimum of three times, with highly reproducible outcomes. The analyses included all collected data without exclusion.

### Reporting summary

Further information on research design is available in the Nature Portfolio Reporting Summary linked to this article.

## Data availability

The raw RNA sequencing data generated in this study are publicly available through GEO database (https://www.ncbi.nlm.nih.gov/geo/query/acc.cgi?acc=GSE283127). All other data generated or analyzed during this study are included in the Article, Supplementary Information, or Source Data file. All data are available from the corresponding authors upon request. Source data are provided with this paper.

## References

1. Ensrud, K. E. & Crandall, C. J. Osteoporosis. *Ann. Intern. Med.* **177**, ITC1–ITC16 (2024).

2. Liu, X. et al. Metal-polyDNA nanoparticles reconstruct osteoporotic microenvironment for enhanced osteoporosis treatment. *Sci. Adv.* **9**, eadf3329 (2023).
3. Fu, H. et al. Acid neutralization and immune regulation by calcium-aluminum-layered double hydroxide for osteoporosis reversion. *J. Am. Chem. Soc.* **144**, 8987–8999 (2022).
4. Guan, H. et al. Magnetic aggregation-induced bone-targeting nanocarrier with effects of piezo1 activation and osteogenic-angiogenic coupling for osteoporotic bone repair. *Adv. Mater.* **36**, e2312081 (2024).
5. Matzkin, E. G., DeMaio, M., Charles, J. F. & Franklin, C. C. Diagnosis and treatment of osteoporosis: what orthopaedic surgeons need to know. *J. Am. Acad. Orthop. Surg.* **27**, e902–e912 (2019).
6. Bellido, T. Bisphosphonates for osteoporosis: from bench to clinic. *J. Clin. Invest.* **134**, e179942 (2024).
7. Zielińska, M. et al. Determination of bisphosphonate properties in terms of bioavailability, bone affinity, and cytotoxicity. *Pharmacol. Rep.* **76**, 1160–1173 (2024).
8. Kuźnik, A., Październiok-Holewa, A., Jewula, P. & Kuźnik, N. Bisphosphonates-much more than only drugs for bone diseases. *Eur. J. Pharmacol.* **866**, 172773 (2020).
9. Gehrke, B., Alves Coelho, M. C., Brasil D'Alva, C. & Madeira, M. Long-term consequences of osteoporosis therapy with bisphosphonates. *Arch. Endocrinol. Metab.* **68**, e220334 (2024).
10. Rossi, F., Perale, G. & Masi, M. *Controlled Drug Delivery Systems: Towards New Frontiers in Patient Care* (PoliMI Springer Briefs, 2016).
11. Sellmeyer, D. E. Atypical fractures as a potential complication of long-term bisphosphonate therapy. *JAMA* **304**, 1480–1484 (2010).
12. Dell, R. M. et al. Incidence of atypical nontraumatic diaphyseal fractures of the femur. *J. Bone Miner. Res.* **27**, 2544–2550 (2012).
13. Duda, G. N. et al. The decisive early phase of bone regeneration. *Nat. Rev. Rheumatol.* **19**, 78–95 (2023).
14. Zhu, G. et al. Bone physiological microenvironment and healing mechanism: Basis for future bone-tissue engineering scaffolds. *Bioact. Mater.* **6**, 4110–4140 (2021).
15. Wong, K. Y., Nie, Z., Wong, M. S., Wang, Y. & Liu, J. Metal–drug coordination nanoparticles and hydrogels for enhanced delivery. *Adv. Mater.* **36**, e2404053 (2024).
16. Wynn, T. A. & Ramalingam, T. R. Mechanisms of fibrosis: therapeutic translation for fibrotic disease. *Nat. Med.* **18**, 1028–1040 (2012).
17. Zheng, N. et al. Magnesium facilitates the healing of atypical femoral fractures: a single-cell transcriptomic study. *Mater. Today* **52**, 43–62 (2022).
18. Wang, Y. et al. Metal-organic frameworks for stimuli-responsive drug delivery. *Biomaterials* **230**, 119619 (2019).
19. Huang, Z. et al. Nanoscale coordination polymers induce immunogenic cell death by amplifying radiation therapy mediated oxidative stress. *Nat. Commun.* **12**, 145 (2021).
20. Xiong, Y. et al. Metal-organic frameworks and their composites for chronic wound healing: from bench to bedside. *Adv. Mater.* **36**, e2302587 (2024).
21. Liu, J. et al. Age-associated callus senescent cells produce TGF-β1 that inhibits fracture healing in aged mice. *J. Clin. Invest.* **132**, 1–17 (2022).
22. Budi, E. H., Schaub, J. R., Decaris, M., Turner, S. & Derynck, R. TGF-β as a driver of fibrosis: physiological roles and therapeutic opportunities. *J. Pathol.* **254**, 358–373 (2021).
23. Su, J. et al. TGF-beta orchestrates fibrogenic and developmental EMTs via the RAS effector RREB1. *Nature* **577**, 566–571 (2020).
24. Ren, L. L. et al. TGF-beta as a master regulator of aging-associated tissue fibrosis. *Aging Dis.* **14**, 1633–1650 (2023).
25. Kim, S. et al. IL-36 induces bisphosphonate-related osteonecrosis of the jaw-like lesions in mice by inhibiting TGF-β-mediated collagen expression. *J. Bone Miner. Res.* **32**, 309–318 (2017).
26. AF, G. et al. Prolonged use of alendronate alters the biology of cranial repair. *Clin. Oral. Investig.* **22**, 1959–1971 (2018).
27. Naidu, A. et al. The effects of bisphosphonates on osteoblasts in vitro. *Oral Surg. Oral Med. Oral Pathol. Oral Radiol. Endodontol.* **106**, 5–13 (2008).
28. Wang, J. et al. Magnesium-pretreated periosteum for promoting bone-tendon healing after anterior cruciate ligament reconstruction. *Biomaterials* **268**, 120576 (2021).
29. Ye Li et al. Biodegradable magnesium combined with distraction osteogenesis synergistically stimulates bone tissue regeneration via CGRP-FAK-VEGF signaling axis. *Biomaterials* **275**, 120984 (2021).
30. Wang, J. et al. Biodegradable magnesium screws accelerate fibrous tissue mineralization at the tendon-bone insertion in anterior cruciate ligament reconstruction model of rabbit. *Sci. Rep.* **7**, 40369 (2017).
31. Mathew, A. A. & Panonnummal, R. Magnesium'—the master cation-as a drug-possibilities and evidences. *Biometals* **34**, 955–986 (2021).
32. Yang, R. et al. Tunable backbone-degradable robust tissue adhesives via in situ radical ring-opening polymerization. *Nat. Commun.* **14**, 6063 (2023).
33. Yang, R. et al. Degradable nanohydroxyapatite-reinforced superglue for rapid bone fixation and promoted osteogenesis. *ACS Nano***18**, 8517–8530 (2024).
34. Zeng, Y., Shih, Y. R. V., Baht, G. S. & Varghese, S. In vivo sequestration of innate small molecules to promote bone healing. *Adv. Mater.* **32**, e1906022 (2020).
35. Tang, J. et al. Flexible osteogenic glue as an all-in-one solution to assist fracture fixation and healing. *Adv. Funct. Mater.* **31**, 2102465 (2021).
36. Liu, C. et al. Bone homeostasis modulating orthopedic adhesive for the closed-loop management of osteoporotic fractures. *Small* **19**, e2302704 (2023).
37. Yao, G. et al. A self-powered implantable and bioresorbable electrostimulation device for biofeedback bone fracture healing. *Proc. Natl. Acad. Sci. USA* **118**, e2100772118 (2021).
38. Debnath, S. et al. Discovery of a periosteal stem cell mediating intramembranous bone formation. *Nature* **562**, 133–139 (2018).
39. Wei, H. et al. Identification of fibroblast activation protein as an osteogenic suppressor and anti-osteoporosis drug target. *Cell Rep.* **33**, 108252 (2020).
40. Chen, Q. et al. A multifunctional composite hydrogel that rescues the ROS microenvironment and guides the immune response for repair of osteoporotic bone defects. *Adv. Funct. Mater.* **32**, 2201067 (2022).
41. Zhu, Q. et al. OTUB1 promotes osteoblastic bone formation through stabilizing FGFR2. *Signal Transduct. Target. Ther.* **8**, 142 (2023).
42. Brown, J. P. Long-term treatment of postmenopausal osteoporosis. *Endocrinol. Metab.* **36**, 544–552 (2021).
43. Wang, G. et al. A catechol bioadhesive for rapid hemostasis and healing of traumatic internal organs and major arteries. *Biomaterials* **291**, 121908 (2022).
44. Tian, Y. et al. Strong biopolymer-based nanocomposite hydrogel adhesives with removability and reusability for damaged tissue closure and healing. *ACS Appl. Mater. Inter.* **14**, 54488–54499 (2022).
45. Horikawa, A., Miyakoshi, N., Shimada, Y., Sugimura, Y. & Kodama, H. A comparative study between intravenous and oral alendronate administration for the treatment of osteoporosis. *Springerplus* **4**, 675 (2015).
46. Zhang, Y. et al. Bioequivalence of generic alendronate sodium tablets (70 mg) to Fosamax® tablets (70 mg) in fasting, healthy volunteers: a randomized, open-label, three-way, reference-replicated crossover study. *Drug Des. Dev. Ther.* **11**, 2109–2119 (2017).
47. Aydin, H. et al. Short-term oral magnesium supplementation suppresses bone turnover in postmenopausal osteoporotic women. *Biol. Trace Elem. Res.* **133**, 136–143 (2010).

48. Li, W., Chi, N., Rathnayake, R. A. C. & Wang, R. Distinctive roles of fibrillar collagen I and collagen III in mediating fibroblast-matrix interaction: a nanoscopic study. *Biochem. Biophys. Res. Commun.* **560**, 66–71 (2021).
49. Sheng, R. et al. Muscle-bone crosstalk via endocrine signals and potential targets for osteosarcopenia-related fracture. *J. Orthop. Transl.* **43**, 36–46 (2023).
50. Florio, M. et al. A bispecific antibody targeting sclerostin and DKK-1 promotes bone mass accrual and fracture repair. *Nat. Commun.* **27**, 11505 (2016).
51. Sun, L. et al. Targeting SOST using a small-molecule compound retards breast cancer bone metastasis. *Mol. Cancer* **21**, 228 (2022).
52. Wang, J. et al. Time-resolved protein activation by proximal decaging in living systems. *Nature* **569**, 509–513 (2019).
53. Chen, Y. et al. Nutrient-delivery and metabolism reactivation therapy for melanoma. *Nat. Nanotechnol.* **19**, 1399–1408 (2024).
54. Reid, I. R. & Billington, E. O. Drug therapy for osteoporosis in older adults. *Lancet* **399**, 1080–1092 (2022).
55. Odvina, C. V. et al. Severely suppressed bone turnover: a potential complication of alendronate therapy. *J. Clin. Endocrinol. Metab.* **90**, 1294–1301 (2005).
56. Ott, S. M. & Heckbert, S. R. Atypical femur fracture risk versus fragility fracture prevention with bisphosphonates. *N. Engl. J. Med.* **383**, 2188–2189 (2020).
57. Schilcher, J., Michaëlsson, K. & Aspenberg, P. Bisphosphonate use and atypical fractures of the femoral shaft. *N. Engl. J. Med.* **364**, 1728–1737 (2011).
58. Zhao, Z. et al. Capturing magnesium ions via microfluidic hydrogel microspheres for promoting cancellous bone regeneration. *ACS Nano***15**, 13041–13054 (2021).
59. Liu, L. et al. The role of magnesium in the pathogenesis of osteoporosis. *Front. Endocrinol.* **15**, 1406248 (2024).
60. Huang, Y. et al. High-strength gelatin hydrogel scaffold with drug loading remodels the inflammatory microenvironment to enhance osteoporotic bone repair. *Adv. Mater.* **37**, e2501051 (2025).
61. Zhu, J. et al. Bioactive poly (methyl methacrylate) bone cement for the treatment of osteoporotic vertebral compression fractures. *Theranostics* **10**, 6544–6560 (2020).
62. Wang, L. et al. Mechanical sensing protein PIEZO1 regulates bone homeostasis via osteoblast-osteoclast crosstalk. *Nat. Commun.* **11**, 282 (2020).
63. Duan, Z. & Lu, H. Effect of mechanical strain on cells involved in fracture healing. *Orthop. Surg.* **13**, 369–375 (2021).
64. Chen, J., Liu, C., You, L. & Simmons, C. A. Boning up on Wolff's law: mechanical regulation of the cells that make and maintain bone. *J. Biomech.* **43**, 108–118 (2010).
65. Saul, D. & Khosla, S. Fracture healing in the setting of endocrine diseases, aging, and cellular senescence. *Endocr. Rev.* **43**, 984–1002 (2022).
66. Armiento, A. R., Hatt, L. P., Sanchez Rosenberg, G., Thompson, K. & Stoddart, M. J. Functional biomaterials for bone regeneration: a lesson in complex biology. *Adv. Funct. Mater.* **30**, 1909874 (2020).
67. Einhorn, T. A. & Gerstenfeld, L. C. Fracture healing: mechanisms and interventions. *Nat. Rev. Rheumatol.* **11**, 45–54 (2015).
68. Fan, W. et al. ECM1 prevents activation of transforming growth factor beta, hepatic stellate cells, and fibrogenesis in mice. *Gastroenterology* **157**, 1352–1367 (2019).
69. Szeto, S. G. et al. YAP/TAZ are mechanoregulators of TGF-beta-smad signaling and renal fibrogenesis. *J. Am. Soc. Nephrol.* **27**, 3117–3128 (2016).
70. You, L., Chen, L., Pan, L., Peng, Y. & Chen, J. SOST gene inhibits osteogenesis from adipose-derived mesenchymal stem cells by inducing Th17 cell differentiation. *Cell Physiol. Biochem.* **48**, 1030–1040 (2018).
71. Liu, Y. et al. Multi-omics characterization reveals the pathogenesis of liver focal nodular hyperplasia. *Iscience* **25**, 104921 (2022).

## Acknowledgements

The authors acknowledge financial support from the National Natural Science Foundation of China (No. 52311530076 to G.X.T.; No. U22A20160 to G.X.T.; No. 110205613 to L.W.; and No. 32471431 to L.Z.), Guangdong Basic and Applied Basic Research Foundation (No. 2023A1515011039 to G.X.T.; No. 2023A1515011738 to T.H.X.; and 2025A1515011845 to L.Z.), the Science and Technology Plan Project of Guangzhou City (No. 2023A03J0383 to L.Z.; No. 2024A03J0935 to T.H.X.; and No. 2024A03J1000 to L.W.), and the Guangzhou Clinical High-Tech Project (No. 2024CL-GX02 to Z.H.W.).

## Author contributions

T.H.X., Z.L.G., and L.Z. designed the research. T.H.X. and D.M.D. synthesized and characterized materials. T.H.X., Z.L.G., and X.D.X. performed biological experiments in vitro. T.H.X., Z.L.G., H.Y., S.L., and X.D.X. established animal models and performed experiments. T.H.X. and Z.L.G. analyzed and graphed data. T.H.X. prepared figures. T.H.X., Z.L.G., and Y.H.J. wrote and edited the manuscript. X.B.Y., G.T., G.X.T., and L.Z. revised the manuscript. T.H.X., Z.H.W., L.W., G.X.T., and L.Z. provided funding. Z.H.W., L.W., X.B.Y., C.Y.N., G.X.T., and L.Z. supervised the project.

## Competing interests

The authors declare no competing interests.

## Additional information

**Supplementary information** The online version contains supplementary material available at https://doi.org/10.1038/s41467-025-60853-8.

**Correspondence** and requests for materials should be addressed to Guoxin Tan or Lei Zhou.

**Peer review information** *Nature Communications* thanks Ling Qin and Jinjin Zhu for their contribution to the peer review of this work. A peer review file is available.